ENDOPHILIN-A2 FUNCTIONS IN MEMBRANE SCISSION IN CLATHRIN-INDEPENDENT ENDOCYTOSIS

Henri-François Renard[1,2,3,*], **Mijo Simunovic**[4,5,*], **Joël Lemière**[6,7,*], **Emmanuel Boucrot**[8], **Maria-Daniela Garcia-Castillo**[1,2,3], **Senthil Arumugam**[1,2,3], **Valérie Chambon**[1,2,3], **Christophe Lamaze**[2,3,9], **Christian Wunder**[1,2,3], **Anne K. Kenworthy**[10], **Anne A. Schmidt**[11], **Harvey T. McMahon**[12], **Cécile Sykes**[6,*], **Patricia Bassereau**[4,*], and **Ludger Johannes**[1,2,3,#]

[1]Institut Curie — Centre de Recherche, Endocytic Trafficking and Therapeutic Delivery group, 26 rue d'Ulm, 75248 Paris Cedex 05, France

[2]CNRS UMR3666, 75005 Paris, France

[3]U1143 INSERM, 75005 Paris, France

[4]Institut Curie — Centre de Recherche, Membrane and Cell Functions group, CNRS UMR 168, Physico-Chimie Curie, Université Pierre et Marie Curie, 26 rue d'Ulm, 75248 Paris Cedex 05, France

[5]The University of Chicaco, Department of Chemistry, 5735 S Ellis Ave, Chicago, IL 60637, USA

[6]Institut Curie — Centre de Recherche, Biomimetism of Cell Movement group, CNRS UMR 168, Physico-Chimie Curie, Université Pierre et Marie Curie, 26 rue d'Ulm, 75248 Paris Cedex 05, France

[7]Université Paris Diderot, Sorbonne Paris Cité, 75205 Paris, France

[8]Institute of Structural and Molecular Biology, University College London & Birkbeck College, London WC1E 6BT, UK

[9]Institut Curie — Centre de Recherche, Membrane Dynamics and Mechanics of Intracellular Signaling group, 26 rue d'Ulm, 75248 Paris Cedex 05, France

[10]Vanderbilt School of Medicine, Department of Molecular Physiology and Biophysics, 718 Light Hall, 37232 Nashville, TN, USA

[11]CNRS, UMR7592, Institut Jacques Monod, Université Paris Diderot, Sorbonne Paris Cité, 15 rue Hélène Brion, 75205 Paris Cedex 13, France

[12]Medical Research Council, Laboratory of Molecular Biology, Cambridge Biomedical Campus, Francis Crick Avenue, CB2 0QH, Cambridge, UK

Abstract

During endocytosis, energy is invested to narrow the necks of cargo-containing plasma membrane invaginations to radii at which the opposing segments spontaneously coalesce, thereby leading to the detachment by scission of endocytic uptake carriers[1]. In the clathrin pathway, dynamin uses mechanical energy from GTP hydrolysis to this effect[2–4], assisted by the BIN/amphiphysin/Rvs (BAR) domain-containing protein endophilin[5,6]. Clathrin-independent endocytic events are often less reliant on dynamin[7], and whether in these cases BAR domain proteins such as endophilin contribute to scission has remained unexplored. Here we found that endophilin-A2 (endoA2) specifically and functionally associates with very early uptake structures that are induced by the bacterial Shiga and cholera toxins, which both are clathrin-independent endocytic cargoes[8]. In controlled *in vitro* systems, endoA2 reshapes membranes prior to scission. Furthermore, we demonstrate that endoA2, dynamin, and actin contribute in parallel to the scission of Shiga toxin-induced tubules. Our results establish a novel function of endoA2 in clathrin-independent endocytosis. They document that distinct scission factors operate in an additive manner, and predict that specificity within a given uptake process arises from defined combinations of universal modules. Our findings finally highlight a previously unnoticed link between membrane scaffolding by endoA2 and pulling force-driven dynamic scission.

Shiga toxin induces the clathrin-independent formation of endocytic plasma membrane invaginations as a first step in its entry into cells[8]. How this highly bent membrane domain is recognized by cellular machinery has remained unexplored. Here, we screened an expression library of curvature-recognizing BAR domain proteins[9] for their localization to these structures. The screen was performed using the receptor-binding B-subunit of Shiga toxin (STxB) on cells with decreased levels of ATP to perturb active cellular machinery that is involved in the processing of these endocytic structures[8,10]. Out of 17 different BAR proteins, only Toca-1, Toca-3, and amphiphysin 2 scored positive (Extended Data Fig. 1a, yellow underlay). However, their siRNA-mediated depletion did not affect STxB trafficking, hence these proteins were not further studied. In cells that expressed exogenous endoA2 (Extended Data Fig. 1a, green underlay), STxB-induced tubules were much shorter (Extended Data Fig. 1b), suggesting a functional crosstalk between endoA2 and the STxB uptake process. Since in non ATP-depleted cells STxB trafficking to the Golgi was not detectably altered by endoA2-GFP expression (Extended Data Fig. 1c), short tubules were most likely the consequence of scission of longer tubules, rather than inhibition of tubule formation.

At the plasma membrane and in very early uptake structures, STxB colocalized with endogenous (Fig. 1a,b) or GFP-tagged endoA2 (Fig. 1c, Extended Data Fig. 2a, and Video V1). Similar colocalization with endogenous endoA2 was observed for the GM1 glycosphingolipid-binding B-subunit of cholera toxin (CTxB) (Fig. 1a), which shares with STxB many aspects related to endocytic membrane bending[11]. Furthermore, the lifetime of structures containing endoA2 strongly increased in the presence of STxB (Extended Data Fig. 2b), and endoA2 was recruited by STxB to the plasma membrane (Extended Data Fig.

2c and Video V2). These results demonstrated that endoA2 localized to sites of STxB and CTxB internalization.

Endophilins have classically been associated with the clathrin pathway (for example Refs.[12]), even if recent studies have indicated that this view may need to be broadened[13,14]. Strikingly, the overlap of endoA2 with fluorescent protein-tagged clathrin or μ2-chain of AP2 was weak, both in transiently transfected HeLa cells, or genome-edited SK-MEL-2 cells (Fig. 1d and Extended Data Fig. 2d,e). STxB also only weakly colabeled with clathrin pathway markers in both cell systems (Extended Data Fig. 2g–j). In contrast, endoA2 extensively codistributed with dynamin (Fig. 1d and Extended Data Fig. 2f), as expected[5,6].

In endoA2-depleted cells, short and apparently tubular STxB-containing invaginations were observed with sizes at the resolution limit of confocal light microscopy (Extended Data Fig. 3a). Using a nanogold conjugate of STxB that was specifically developed for this study (Extended Data Fig. 3b,c), it could be shown by electron microscopy that these structures were connected to the plasma membrane (Fig. 2a and Extended Data Fig. 3d). Their frequency did not increase upon depletion of endoA2 (Fig. 2b, left), while their average length significantly increased (Fig. 2b, right). These findings were strongly in favor of a function for endoA2 in scission of STxB-induced endocytic plasma membrane invaginations.

Retrograde STxB trafficking to TGN/trans-Golgi membranes in endoA2-depleted cells was quantified using a STxB variant with tandem protein sulfation sites, termed STxB-Sulf$_2$. With different siRNAs that had variable depletion efficiencies (Extended Data Fig. 4a), we found that sulfation of STxB-Sulf$_2$ in trans-Golgi/TGN membranes was inhibited in a dose-dependent manner with cellular endoA2 levels (Fig. 2c), while STxB cell surface binding was not affected (Extended Data Fig. 4b). Depletion of the TGN-localized tSNARE protein syntaxin-16 served as a benchmark treatment[15]. We concluded that endoA2 was required for efficient STxB trafficking into cells. A similar conclusion was reached when CTxB endocytosis was analyzed in endoA2-depleted BSC-1 cells (Extended Data Fig. 4c).

In endoA2-depleted cells, the inhibition of STxB transport to Golgi membranes could also be documented by immunofluorescence (Fig. 2d). Expression of siRNA-resistant endoA2 or of a SH3 domain deletion mutant (SH3) rescued this phenotype (Fig. 2d and Extended Data Fig. 4d), suggesting that the function of endoA2 in STxB trafficking was independent of SH3 domain interaction with binding partners such as dynamin. In contrast, a N-terminal amphipathic helix deletion mutant (endoA2 H0) failed to rescue STxB trafficking (Fig. 2d and Extended Data Fig. 4d), likely due to a role of this helix in membrane recruitment (see below). Correspondingly, endoA2 SH3 expression reduced STxB-induced tubule length on ATP-depleted cells, similar to wild-type endoA2, while endoA2 H0 failed to do so (Extended Data Fig. 4e), reinforcing the hypothesis of endoA2 participating in membrane scission.

Depletion of endoA2 did not affect transferrin internalization or recycling, the steady state localization of the clathrin cargo proteins TGN46 and cation-independent mannose 6-phophate receptor[16,17], or anterograde transport of E-cadherin (Extended Data Fig. 5a–c).

Clearly, it was the cellular entry of STxB and CTxB that was specifically altered under these conditions. In contrast, depletion of the μ2-chain of the clathrin adaptor AP2 had no effect on STxB trafficking, while transferrin uptake was efficiently blocked (Extended Data Fig. 5d,e).

To address the function of endoA2 in scission, we exploited the knocksideways system[18] to acutely and reversibly remove endoA2 from its normal site of action at the plasma membrane. HeLaM cells were used that expressed i) the mitochondrial trap construct Mito-YFP-FRB, and ii) endoA2 tagged with both, GFP and the rapamycin-binding protein FKBP. In cells with reduced ATP levels, the length of STxB-induced tubules was only slightly increased upon depletion of endogenous endoA2 (Fig. 3a and Extended Data Fig. 6a), due to the presence of the siRNA-resistant FKBP-tagged endoA2 fusion protein. The fusion protein was then sequestered on mitochondria by addition of rapamycin, upon which the length of STxB containing tubules significantly increased (Fig. 3a and Extended Data Fig. 6a). This effect was reversible, as rapamycin washout led to significantly shorter tubules (release condition). These results strongly reinforced the idea that endoA2 is involved in the scission of STxB-induced endocytic invaginations.

Controlled model membrane systems were then used to dissect aspects of endoA2 function with respect to membrane tubulation and scission. Cell-sized liposomes that reproduced a key aspect of natural membranes, i.e. an asymmetric bilayer composition, were obtained *via* the inverse emulsion technique[19] (see Methods section for leaflet compositions). To permit the acute introduction of endoA2 into the system, its topology was inverted with respect to the cellular situation: when indicated, STxB was included inside liposomes, whereas endoA2 was added in the external medium. Incubation with up to 4 μM endoA2 did not lead to the formation of tubules (Fig. 3b, condition i). In contrast, liposomes that contained STxB exhibited coiled tubular protrusions (condition ii). Addition of endoA2 to STxB-containing liposomes at concentrations of 2 (Fig. 3b, condition iii) or 4 μM (condition iv) caused tube straightening. Thus, endoA2 prompted the morphological transformation of STxB-induced tubular membranes.

For dynamic measurements, we turned to another setup in which optical tweezers were used to mechanically pull membrane tethers from giant unilamellar vesicles, held with a micropipette[20]. The force exerted by protein binding onto the tether membrane could be directly measured, tube radii controlled in a range from 10 nm to 100 nm, and tube elongation driven at controlled velocities. Upon endoA2 injection at concentrations as low as 1 μM (protein concentration inside the injection pipette), the tube retraction force decreased to zero (Fig. 3c), indicating the formation of an external scaffold on the tether membrane, which likely explained the morphological transformation in the asymmetric bilayer system.

We did not observe spontaneous scission of endoA2-scaffolded tubes (*n* = 35). However, when these were pulled further at elongation rates of ~0.5 μm/s, the tube retraction force increased (Fig. 3d), leading to breakage in 15 out of 18 cases (Fig. 3e). Elongation of bare tethers from fluid membranes, at rates as those used in this study, never leads to scission[19,21], and we explicitly confirmed the resilience of bare tubes on forced elongation at

an elevated rate of ~10 μm/s (n=2). We speculate that interactions between endoA2 scaffold and underlying lipids limit the flow of lipids upon tube extension, thereby leading to increased membrane tension and spontaneous squeezing of the tube until the scission threshold radius has been reached.

The pulling speed that was required *in vitro* to induce the scission of endoA2-scaffolded tubes was very similar to the speed produced by microtubule-based molecular motors[22], and microtubules have previously been implicated in the cellular entry of Shiga toxin[23]. Interference with microtubule-based functions prior to reduction of cellular ATP levels led to the loss of long STxB-induced tubules (Extended Data Fig. 6b,c), while short (< 200 nm) tubules persisted (Extended Data Fig. 7). These findings suggested that STxB-induced invaginations were recognized by molecular motors for the further processing into cells.

As indicated by a change in tube retraction force, the endoA2 H0 mutant formed a scaffold only at concentrations above 7 μM (Extended Data Fig. 6d), seven times higher than the minimum concentration required for wild-type endoA2. Furthermore, the radius of the endoA2H0 scaffold was on average twice that of the wild-type endoA2 (23 nm ± 10 nm, n = 10 versus 12 nm ± 4 nm, n = 6, respectively). When pulled, endoA2 H0-scaffolded tubes nevertheless underwent scission in 5 out of 5 cases (Extended Data Fig. 6e). The N-terminal amphipathic helix thus did not play a decisive role in scission by elongation of scaffolded membrane tubes. Rather, it seemed important for efficient recruitment of endoA2 to the membrane, as well as possibly affecting the molecular organization of the scaffold.

We next investigated the role of endoA2 in concert with other scission factors that have been shown before to play a role in STxB uptake. The first was actin[10]. EndoA2 and actin strongly and dynamically colocalized (Extended Data Fig. 8a), and even in endoA2-depleted cells actin was localized on STxB-induced membrane invaginations (Extended Data Fig. 8b,c). This indicated that endoA2 was not required for actin recruitment to STxB uptake structures. Interestingly, the depletion of endoA2 or the depolymerization of actin with 0.5 μM latrunculin-A led to a similar increase in the length of STxB-induced tubules, and the concomitant treatment had an additive effect (Fig. 4a and Extended Data Fig. 8d,e). Thus, both endoA2 and actin contributed independently to scission probability in STxB endocytosis. In cells that were depleted of ARPC2 (p34 subunit of the Arp2/3 complex) the length of STxB-induced tubules was similar to that observed in latrunculin-A treated cells (Fig. 4a and Extended Data Fig. 8f), confirming the specificity of our observations.

Upon depletion of dynamin, STxB-induced tubules were longer than in control cells[8] (Fig. 4a), and endoA2 was clearly localized on these structures (Extended Data Fig. 9a, lower panel). Tubules positive for endogenous endoA2 (Extended Data Fig. 9b) were seen only in the presence of STxB (compare ± STxB panels), in line with our model membrane results. This finding documented that these tubules did not preexist but were indeed induced by STxB. Dynamin was still found in association with STxB uptake structures in endoA2-depleted cells (Extended Data Fig. 9c), indicating that in addition to endoA2, other proteins contribute to dynamin recruitment to membranes[24]. As for actin, concomitant depletion of dynamin and endoA2 had an additive effect on the length of STxB-induced tubules (Fig. 4a and Extended Data Fig. 9d).

Actin, dynamin, and endoA2 thus independently contributed to the probability of scission in the STxB uptake pathway. Indeed, when dynamin and endoA2-depleted cells were concomitantly incubated with 0.25 μM latrunculin-A, tubule length increased further, leading to an unprecedented tubulation phenotype throughout the cell population (Fig. 4a and Extended Data Fig. 9d). Importantly, when STxB-induced tubules were binned according to their length (Fig. 4b), a frequency shift was observed when going from unperturbed cells (A condition, red) to cells submitted to single (B condition, yellow), double (E condition, green), or triple (H condition, blue) perturbation. This data representation clearly illustrated that short tubules (most abundant in unperturbed cells) were progressively transformed into long tubules (most abundant in the triple perturbation condition).

Protein biosynthesis inhibition is an established measure of Shiga toxin arrival in the cytosol[25]. Cells that were depleted of endoA2 or dynamin, or were incubated with 0.25 μM of latrunculin-A were only weakly protected against Shiga-like toxin-1 (STx-1; note that STx-1 and Shiga toxin differ in only one residue) (Fig. 4c and Extended Data Fig. 10a–c). These individual treatments thus failed to impose a transport block that would shut down access to the cytosol to levels that were required to be robustly detected by this extremely sensitive method. In contrast, triple treatment induced a substantial shift to the right of the intoxication curves (Extended Data Fig. 10d), such that 5.0-fold ($\pm$ 0.9, n=4) more STx-1 was required to achieve the same level of protein biosynthesis inhibition as in control conditions (see quantification in Fig. 4c). Clearly, the scission factors endoA2, actin, and dynamin needed to be inhibited simultaneously for a substantial protection of cells against STx-1.

Our study reveals a novel function of endoA2 in clathrin-independent endocytosis of Shiga and cholera toxin, and suggests more generally that this BAR domain protein operates preferentially on non-clathrin sites of uptake. Our data also provides strong evidence for a function of endoA2 in the scission process. In the context of the Shiga toxin model, endoA2 is the first cellular factor that was identified to specifically recognize the mechanical signal transmitted by the toxin to the cytosol: a highly curved plasma membrane domain. Unexpectedly, our findings suggest that actin[10] and dynamin[8] contribute in an additive manner with endoA2 to scission in Shiga toxin uptake. They likely act on the same endocytic invaginations and not on parallel uptake events, since the overall length of Shiga toxin-nduced plasma membrane tubules strongly increased in cells in which all three scission factors were inhibited. Such additive function in scission is unexpected and suggests that specificity within given endocytic processes is the result of defined cocktails of modular machinery. This hypothesis does not exclude a functional interaction between scission factors[26,27]. An exciting new modality emerges from our observations that scaffolding by endoA2 sensitizes tether membranes for pulling force-induced scission. This finding should stimulate further research into the function of cytoskeleton-based molecular motors in scission and the mechanisms by which coating by BAR domain proteins prime membranes to this effect.

Methods

Antibodies and other reagents

The following antibodies were purchased from the indicated suppliers: rabbit polyclonal anti-endoA2 for Western blotting (Bethyl, cat.# A302–349A, 1/2000) or immunofluorescence and cryo-electron microscopy (Santa Cruz Biotechnology, cat.# sc-25495, 1/200 for immunofluorescence and 1/10 for cryo-electron microscopy); rabbit polyclonal anti-STxB (Covalab, 1/100 for cryo-electron microscopy); mouse monoclonal anti-clathrin heavy chain for Western blotting (BD Biosciences, cat.# 610500, 1/5000); mouse monoclonal anti-α-tubulin (Sigma, cat.# T5168, 1/5000 for Western blotting); rabbit polyclonal anti-syntaxin-16 (Synaptic Systems, cat.# 110 163, 1/1000 for Western blotting); rabbit monoclonal anti-giantin (Institut Curie, recombinant proteins platform, cat.# A-R-R#05, 1/100 for immunofluorescence); sheep polyclonal anti-TGN46 (Serotec, cat.# AHP500G, 1/200 for immunofluorescence); mouse monoclonal anti-CI-MPR (Abcam, cat.# ab2733, 1/200 for immunofluorescence); rabbit polyclonal anti-mCherry (Institut Curie, Plateforme protéines recombinantes, cat.# A-P-R#13, 1/200 for immunofluorescence); mouse monoclonal anti-GFP (Roche Applied Sciences, cat.# 11 814 460 001, 1/1000 for Western blotting); mouse monoclonal anti-dynamin Hudy 1 (Upstate, cat.# 05–319, 1/200 for immunofluorescence); mouse monoclonal anti-dynamin (BD Biosciences, cat.# 610246, 1/1000 for Western blotting); rabbit polyclonal anti-ARPC2 (Millipore, cat.# 07–227, 1/1000 for Western blotting); rabbit polyclonal anti-DYNC1H1 (Proteintech, cat.# 12345-1-AP, 1/200 for Western blotting); secondary antibodies conjugated to Alexa 488, Cy3, Cy5, AMCA or HRP (Beckman Coulter and Invitrogen). The mouse monoclonal anti-STxB antibody 13C4 was purified from hybridoma cells (ATCC CRL-1794), and the mouse monoclonal anti-clathrin heavy chain antibody X22 (used at 1/1000 for immunofluorescence) was a gift from Elizabeth Smythe. 2-deoxy-D-glucose, sodium azide, latrunculin-A and nocodazole were purchased from Sigma.

Cell culture

HeLa and BSC-1 cells were grown at 37°C under 5% CO_2 in DMEM high glucose Glutamax (Invitrogen) supplemented with 10% FCS, 0.01% penicillin-streptomycin, and 5 mM pyruvate. Genome-edited SK-MEL-2 expressing RFP-tagged clathin light chain were kindly provided by David Drubin (University of California, Berkeley), and were grown at 37°C under 5% CO_2 in DMEM/F12 (Invitrogen) supplemented with 10% FCS, 0.01% penicillin-streptomycin, and 5 mM pyruvate. HeLaM cells stably expressing Mito-YFP-FRB were kindly provided by Margaret S. Robinson (Cambridge Institute for Medical Research). These were grown at 37°C under 5% CO_2 in DMEM high glucose Glutamax (Invitrogen) supplemented with 10% FCS, 0.01% penicillin-streptomycin, 5 mM pyruvate, and 137.5 μg/ml hygomycine B. HeLaM Mito-YFP-FRB cells stably expressing C-terminally GFP-FKBP-tagged rat endoA2 were generated for this study (see below) and grown in the same medium than the mother cells, supplemented with 0.5 mg/ml G418.

Depletion of cellular ATP

Cellular ATP was depleted as previously described[8,28]. Briefly, cells were incubated for 15 to 20 min at 37°C in PBS^{++} supplemented with 10 mM 2-deoxy-D-glucose and 10 mM NaN$_3$.

DNA constructs and transfection

Expression plasmids for C-terminally GFP-tagged rat endoA2 (Pietro De Camilli), mCherry-tagged µ2 adaptin (Christian Merrifield), mRFP-tagged dynamin-2 or clathrin light chain (Tom Kirchhausen) were kindly provided by the indicated colleagues.

A bicistronic vector encoding SBP-mCherry-E-cadherin and KDEL-streptavidin, used for the anterograde E-cadherin transport assay, was kindly provided by Franck Perez, and a plasmid encoding mCherry-LifeAct[29,30] by Philippe Chavrier.

GFP-tagged mutants of endoA2 (H0 lacking N-terminal amphipatic H0 helix, and SH3 lacking C-terminal SH3 domain) were obtained by PCR from full-length endoA2.

For knocksideways with endoA2, a C-terminally GFP-FKBP-tagged rat endoA2 construct was engineered. For this, rat endoA2-GFP and the FKBP sequence bearing a stop codon were amplified by PCR from plasmids (for amplification of endoA2-GFP fragment, forward primer was 5'-ATACTTAAGATGTCGGTGGCGGGGCTGAAG-3' and reverse primer was 5'-TTCCACCTGCACTCCCATCCCTCCGCCCTTGTACAGCTCGTCCAT-3'; for amplification of FKBP fragment, forward primer was 5'-ATGGACGAGCTGTACAAGGGCGGAGGGATGGGAGTGCAGGTGGAA-3' and reverse primer was 5'-AGTGCGGCCGCTTATTCCAGTTTTAGAAGCTC-3'). The PCR fragments were designed in such a way that they possessed overlapping sequences. This allowed obtaining an endoA2-GFP-FKBP fragment via a third PCR on the two previous fragments with appropriate primers (forward primer from endoA2-GFP amplification: 5'-ATACTTAAGATGTCGGTGGCGGGGCTGAAG-3'; reverse primer from FKBP fragment amplification: 5'-AGTGCGGCCGCTTATTCCAGTTTTAGAAGCTC-3'). After insertion in a pIRESneo2 vector between AflII and NotI restriction sites, clones were validated by sequencing.

For immunofluorescence and live cell imaging experiments, plasmids were transfected with FuGene 6 (Promega) according to the manufacturer's instructions, or using the classical calcium phosphate procedure[31]. Cells were used for experiments 16 to 24 hours after transfection. For the production of a HeLaM Mito-YFP-FRB cell line stably expressing endoA2-GFP-FKBP, the pIRESneo2/endoA2-GFP-FKBP plasmid was transfected by electroporation, and clones were selected with 0.5 mg/ml G418.

RNA interference

Most siRNAs used in this study were purchased from Qiagen and transfected with HiPerFect (Qiagen) according to manufacturer's instructions. Experiments were performed 72 hours after siRNA transfection, where protein depletion efficiency was maximal as shown by immunoblotting analysis with specific antibodies (routinely 80–90%). For most experiments, cells were replated 24 hours before use, according to the need of the

experiment. AllStars Negative Control siRNA served as a reference point. The depletion of endoA2 was achieved with three different sequences at final concentrations between 2 to 10 nM: #5 (ref. SI03057250: 5'-CACCAGCAAGGCGGTGACAGA-3'), #7 (ref. SI03073931: 5'-CATGCTCAACACGGTGTCCAA-3') and #8 (ref. SI03108049: 5'-TACACTAGCGCTGACTCCCAA-3'). For syntaxin-16 depletion, a custom-made siRNA sequence[15] at concentrations between 2 to 10 nM (5'-AAGCAGCGATTGGTGTGACAA-3'); for dynamin-2, a single siRNA at 10 nM (ref. SI02654687: 5'-CTGCAGCTCATCTTCTCAAAA-3'); for α-adaptin, a single siRNA sequence[32] at concentrations between 10 to 40 nM (5'-AAATGGCGGTGGTGTCGGCTC-3', Dharmacon); for ARPC2, a smartpool of 4 siRNA sequences (ref. L-012081-00, Dharmacon: 5'-CCATGTATGTTGAGTCTAA-3', 5'-GCTCTAAGGCCTATATTCA-3', 5'-GGACAGAGTCACAGTAGTC-3', 5'-GTACGGGAGTTTCTTGGTA-3') at 40 nM.

For endoA2 depletion from BSC-1 cells, a single all Stealth siRNA was used (ref. HSS109705, Invitrogen: 5'-GCTGACCAACCAGATCGATGAGAAC-3'). Cells seeded on 12 mm coverslips placed in 24 well plates (for microscopy) or on glass-bottom 96 well plates (plate reader experiments) were transfected twice (on day 1 and 2) with Oligofectamine (Life Technologies) complexed to 8 or 1.6 pmol, respectively, of HSS109705 siRNA and analyzed on day 4 (72 hours after the first transfection).

Recombinant proteins

Recombinant wild-type STxB, STxB-Cys, and STxB-Sulf$_2$ were purified from bacterial periplasmic extracts as previously described[33]. C-terminally Strep-tagged mouse endoA2 and endoA2 ΔH0 (N-terminal amphipatic helix deletion mutant) were expressed in bacteria and purified on Strep-Tactin column (IBA), as previously described[34]. For more details, see Supplementary Information section.

Light microscopy

For immunofluorescence studies, cells were maintained at 37°C during the full duration of the experiment and during fixation (4% paraformaldehyde) to preserve the integrity of STxB-induced tubules. After quenching with 50 mM NH$_4$Cl and permeabilization with saponin (0.5% saponin, 2% BSA in PBS), cells were incubated with primary and secondary antibodies, and mounted with Mowiol.

Fixed samples were imaged with a Nikon A1r confocal microscope equipped with a CFI Plan Apo VC 60X NA 1.4 oil immersion objective, when not specified otherwise. Wild field images were acquired on a Leica DM 6000B epifluorescence inverted microscope equipped with a HCX PL Apo 63X NA 1.40 oil immersion objective and an EMCCD camera (Photometrics CoolSNAP HQ). Super resolution images were acquired on a N-SIM (Structured Illumination Microscopy, Nikon) equipped with a CFI Apo TIRF 100X NA 1.49 oil immersion objective and an EMCCD camera (Photometrics CoolSNAP HQ2).

For live cell imaging, cells were grown to subconfluence on FluoroDish chambers with integrated glass coverslips (World Precision Instruments). All observations were made at 37°C and 5% CO$_2$. Different imaging devices were used. Plasma membrane images were

acquired on a TIRF video microscope (Nikon) equipped with a CFI Apo TIRF 100X NA 1.49 oil objective and an EMCCD camera (Photometrics HQ2). Other live cell images were acquired on spinning disk confocal devices (Nikon) equipped with EMCCD cameras (Photometrics CoolSNAP HQ2). Montages, kymographs, and movies were prepared with ImageJ or Fiji (NIH) and MetaMorph Software.

Electron microscopy

Two different cell embedding techniques were used: cryo-protection and epon. For further details, see Supplementary Information section.

STxB sulfation

The sulfation assay was performed as previously described[35]. For further details, see Supplementary Information section.

CTxB internalization

Alexa555-labelled CTxB (Life Technologies) was used at 0.9 to 5 nM (50 to 285 ng/mL) and incubated on cells directly at 37°C and 5% CO_2 (without pre-incubation on ice) for up to 10 min. Following incubation, samples destined for microscopy were quickly washed once and fixed at 37°C with pre-warmed 3.7% PFA in PBS (20 min, 37°C). Samples were then washed (twice with PBS and one with 50 mM NH4Cl in PBS), immunostained and imaged on a laser scanning confocal microscope (TCS Sp5 AOBS; Leica). For CTxB uptake assay, cells grown in 96-well glass bottom black plates (Thermo Scientific) were incubated with 5 nM toxin for 10 min at 37°C, moved on ice to stop further endocytosis, washed once with ice-cold PBS to remove unbound toxin and twice with an ice-cold low pH solution (300 mM NaCl, 5 mM KCl, 1 mM $CaCl_2$, 1 mM $MgCl_2$, 0.2 M acetic acid, pH 2.5, as described in Refs[36,37]), which removed 90 +/− 6 % of the cell surface signals (n=3, p<0.0001, two tailed t-test) as compared to samples incubated with the toxin on ice (surface staining). The samples were then further washed twice with ice-cold PBS (to increase the pH back to 7.4) and finally fixed on ice with 3.7% PFA for 30 min. Cells were then washed twice with PBS and once with 50 mM NH_4Cl in PBS and incubated with DAPI to label their DNA (used to normalize the number of cells in between samples and experiments). Signals from internalized CTxB-A555 (protected from the acid wash) and DAPI were measured using a plate reader (FLUOstar Optima, BMG).

Intoxication

The intoxication assay with STx-1 holotoxin was performed as previously described[38]. For further details, see Supplementary Information section.

Knocksideways

The knocksideways technique was adapted to endoA2, as described[39]. For further details, see Supplementary Information section.

Flow Cytometry

siRNA transfected or PPMP treated cells (as control) were detached using 4 mM EDTA and incubated for 30 min on ice with Tf-A647 (10 μg/ml) and STxB-cystein-Alexa488 (1 μM) in PBS^{++} containing 0.2% BSA. After washing in ice-cold PBS, fluorescence was measured with a LSR-II flow cytometer (BD Biosciences). Single stained samples were used to verify that the fluorescence from each fluorophore was only detected in the expected channel.

Transferrin endocytosis

The endocytosis assay was performed essentially as previously described[35]. For further details, see Supplementary Information section.

Transferrin recycling

Cells were incubated for 40 min at 37°C with Tf-SS-biot (60 μg/ml) in PBS^{++} supplemented with 5 mM glucose and 0.2% BSA. After washing, cells were aliquoted (150,000 cells per data point) and placed for the indicated times at 37°C in PBS^{++} supplemented with 5 mM glucose and 0.2% BSA in the presence of a 50-fold molar excess of non-biotinylated holo-Tf (Sigma-Aldrich). The cells were placed on ice, washed in PBS^{++}, and lysed in 10 mM Tris-HCl pH 7.4, 50 mM NaCl, 1 mM EDTA, 0.2% BSA, 0.1% SDS, 1% Triton X-100. The amount of cell-associated biotinylated Tf was determined by ELISA, as in the endocytosis assay.

Anterograde E-cadherin transport

The Retention Using Selective Hooks (RUSH) system was used to quantify anterograde transport of E-cadherin, as previously described[40]. For further details, see Supplementary Information section.

Asymmetric liposomes produced by inverted emulsion

Lipids and reagents—Egg phosphatidylcholine (EPC), cholesterol (Chol), L-α-phosphati-dylinositol-4,5-bisphosphate (PI(4,5)P2) and brain total lipid extract (BE) were purchased from Avanti Polar Lipids (Alabaster, AL, USA). Ceramide trihexosides (Gb3) was purchased from Matreya LLC (Pleasant Gap, PA, USA). All chemicals, including mineral oil were purchased from Sigma Aldrich (St Louis, MO, USA) unless specified otherwise.

Buffer composition—Inside buffer: 25 mM HEPES pH 7.4, 100 mM NaCl, 0.5 mM EGTA, and 75 mM sucrose. Outside buffer: 25 mM HEPES pH 7.4, 100 mM NaCl, 0.5 mM EGTA, 0.05 mg/ml β-casein, and 75 mM glucose.

Liposome preparation—Asymmetric liposomes were obtained using an inverted emulsion technique[41,42]. Lipids were dissolved in mineral oil at a total concentration of 0.5 mg/ml, with a composition of EPC/Chol/Gb3 at a molar ratio of 65:30:5 (inner leaflet) or of BE/PI(4,5)P2 at a mass ratio of 95:5 (outer leaflet). A volume of 2.5 ml of each oil-lipid mixture was sonicated in a bath at 35°C for 30 min at a power of 30 W, cooled and stored for one day at room temperature. A volume of 30 μl of the outer leaflet oil-lipid mixture was

poured in a tube on top of the same volume of the outside buffer. The tube was left at room temperature for at least 2 hours. In the mean time, an emulsion was obtained by mixing a volume of 250 μl of inner leaflet oil-lipid mixture with 1.25 μl of inside buffer (with or without proteins) and by pumping back-and-forth with a syringe. Then, 50 μl of this emulsion was slowly added to the top phase of the tube and immediately centrifuged at 250×g for 5 min. Asymmetric liposomes were thus obtained at the bottom of the tube and were collected by removing the upper oil phase.

Liposome observation—Liposomes were observed with an IX70 Olympus inverted microscope equipped with a Olympus 100 oil-immersion phase-contrast objective, NA 1.35 (Olympus, Tokyo, Japan). Fluorescent Shiga toxin was excited by a 200 W mercury lamp (OSRAM, Munich, Germany). Images were acquired with a cooled CCD camera CoolSNAP ES (Photometrics, Tucson, USA).

Preparation of giant unilamellar vesicles, tether-pulling experiments, and data analysis

Reagents—Brain total lipid extract, 1,2-distearoyl-*sn*-glycero-3-phosphoethanolamine-N-[biotinyl(polyethyleneglycol)-2000] (DSPE-PEG(2000)-biotin), and L-α-phosphatidylinositol-4,5-bisphosphate (PI(4,5)P2) were purchased from Avanti Polar Lipids. BODIPY-TR-C5-ceramide was obtained from Molecular Probes. All reagents used to make buffers and β-casein from bovine milk (>99%) were purchased from Sigma-Aldrich.

Preparation of giant unilamellar vesicles (GUVs)—GUVs were prepared by electroformation on Pt-wires. Approximately 5 μL of the lipid mix, containing ~95% brain total extract, 5% PI(4,5)P2, ~0.3% DSPE-PEG(2000)-biotin, and 0.5% BODIPY-TR-C5-ceramide (all molar fractions), was deposited on Pt-wires, at 3 g/L, and dried under vacuum for an hour. GUVs were grown overnight in a mixture of 200 mM sucrose, 50 mM NaCl, 20 mM HEPES (pH=7.4), at $v = 500$ Hz, $I = 0.25$ V, $t = 4$ °C.

Tether-pulling experiments—An experimental chamber, consisting of two parallel cover slips, spaced a few millimeters from each another, was immersed in a 5 g/L solution of β-casein for 30 min in order to passivate the glass surface. The chamber was filled with 5–10 μL of the electroformation solution and 200 μL buffer solution (200 mM glucose, 50 mM NaCl, 20 mM HEPES at pH = 7.4). The chamber was sealed with oil after ~10 min to prevent evaporation. GUVs with visible fluctuations were aspirated in a micropipette. Membrane tension was controlled via the aspiration pressure. A tether was created by bringing in contact the GUV with a streptavidin-coated polystyrene bead, approximately 3 μm in diameter (Spherotec), trapped with optical tweezers. Using another micropipette, endoA2 was injected in the vicinity of the GUV (at bulk concentrations in the micropipette 0.3–5 μM per monomer for the wild-type and 5.0–7.0 μM for the endoA2 H0 mutant). The force measurements were then repeated.

Pulling-force induced fission—After a scaffold has formed, confirmed with the drop in force, the source of the protein was removed and the tether was further elongated at a rate of 0.5 μm/s.

Tube radius measurements—The radius of the tube was determined from the intensity of the fluorescence signal of the tube, considering that the ratio of fluorescence intensities of lipids inside the tube and inside the vesicle is proportional to the surface of the tube. To get absolute values, we used a normalization factor determined in Ref[43].

Image quantifications

All image quantifications were performed with ImageJ or Fiji (NIH) and Matlab (MathWorks).

Quantification of STxB transport to the Golgi apparatus—Z-stacks were acquired on images of cells in defined experimental conditions. STxB-Cy3 fluorescence intensities were measured with ImageJ software (NIH) on z-projections, either from the entire cell, or from the Golgi region, as defined by Giantin labeling. The ratio was then calculated as an index of Golgi localization.

Quantification of Tf-A488 endocytosis—The mean intensity of Tf-A488 fluorescence in the cell area was measured with ImageJ software (NIH) as above on z-projections, after background correction. Mean fluorescence intensities of control conditions were considered as 100%.

Quantification of colocalization on TIRF images—In order to quantify the colocalization between two channels, an object-based method was used, as implemented in JACoP[44], based on the coincidence between two centroids with a 0.5 pixel tolerance. This was achieved in an ImageJ macro by first segmenting the tagged proteins by spot detection in each channel, finding their position, and growing them by dilation to 0.5 pixel radius. The spot detection consisted in finding maxima on the smoothed image (3×3 average filter) using the 'find maxima' plugin of ImageJ whose noise tolerance parameter was set up visually independently for each channel. The results were expressed as the percentage of colocalized spots over the total number of spots in the red and the green channel, respectively.

Quantification of endoA2-GFP recruitment to the plasma membrane—Spinning disk time series at fixed z-positions were acquired for 80 sec at 37°C with 0.84 sec intervals and an exposure time of 80 ms for each channel. STxB was added 15 sec after the beginning of each time series. Images were then treated with Fiji. Plasma membrane segments were selected randomly and linear regions of interest (ROI) were drawn. The mean fluorescence along ROI was measured in each channel over all images of a time series. Data were plotted for fluorescence intensity (in percent of maximum intensity) over time (in sec).

Quantification of endoA2 spot lifetime—Kymographs were obtained from image stacks using MetaMorph Software. Kymographs were processed using a first Fiji macro. The first step consisted in the creation of background images that were subtracted from the original images. Background images were obtained using the 'Remove Outliers' plugin with a 5-pixel radius and a 50 grey level threshold. An automatic threshold was then proposed and adjusted visually to select the tracks. Selected tracks were saved in ROI files for each image. A second macro was then used to measure the length of tracks, with a step allowing

manual correction of ROI, if required. The lifetime of each structure was extracted from the length of the bounding boxes of the segmented tracks in the kymographs, corresponding to their length in frames.

Quantification of STxB-induced tubule length—The quantification of STxB-induced tubule length was achieved in batch for all images by segmenting the tubular structures and skeletonising them so that the number of pixels of tubules was proportional to their length. For this, we used a Fiji macro based on the enhancement of tubular structures by computing eigenvalues of the hessian matrix on a Gaussian filtered version of the image (sigma = 1 pixel), as implemented in the tubeness plugin. The tubules were then thresholded and structures containing less than 3 pixels were discarded. A visual check was performed and a manual correction of segmented tubules was done, if required. The segmented and corrected structures were then reduced to a 1-pixel thick skeleton, using the Fiji plugin "skeletonize". Data were grouped by conditions and the length of skeletonized tubules in pixels was converted in micrometer units using Matlab (MathWorks).

Statistical analyses

All statistical analyses were performed using Prism v4.0 software (Graphpad Inc., San Diego, CA). Data were tested for Gaussian distribution with Kolmogorov-Smirnov test (with Dallal-Wilkinson-Lillie for P-value). In case of non-Gaussian distribution, nonparametric tests were carried on: two-tailed Mann-Whitney U test if there were only two conditions to compare, one-way ANOVA (Kruskal-Wallis test) with a Dunn's test if there were more than two data groups to compare. In case of Gaussian distribution, parametric tests were carried on: two-tailed t-test for the comparison of the means if there were only two conditions to compare, parametric one-way ANOVA with a Bonferroni test if there were more than two data groups to compare. Significance of mean comparison is represented on the graphs with asterisks. All error bars are corresponding to standard error of the mean (SEM).
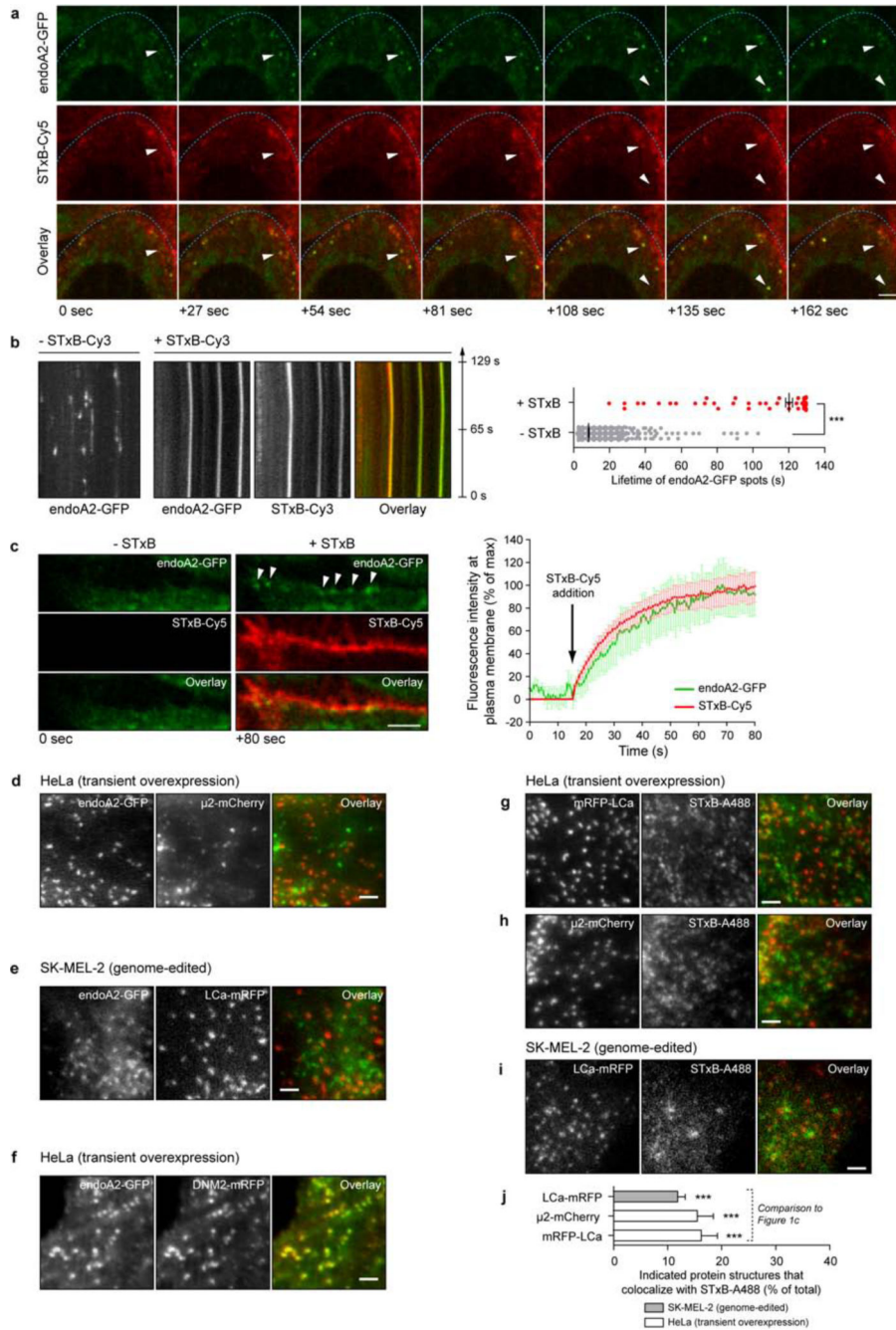
Extended Data
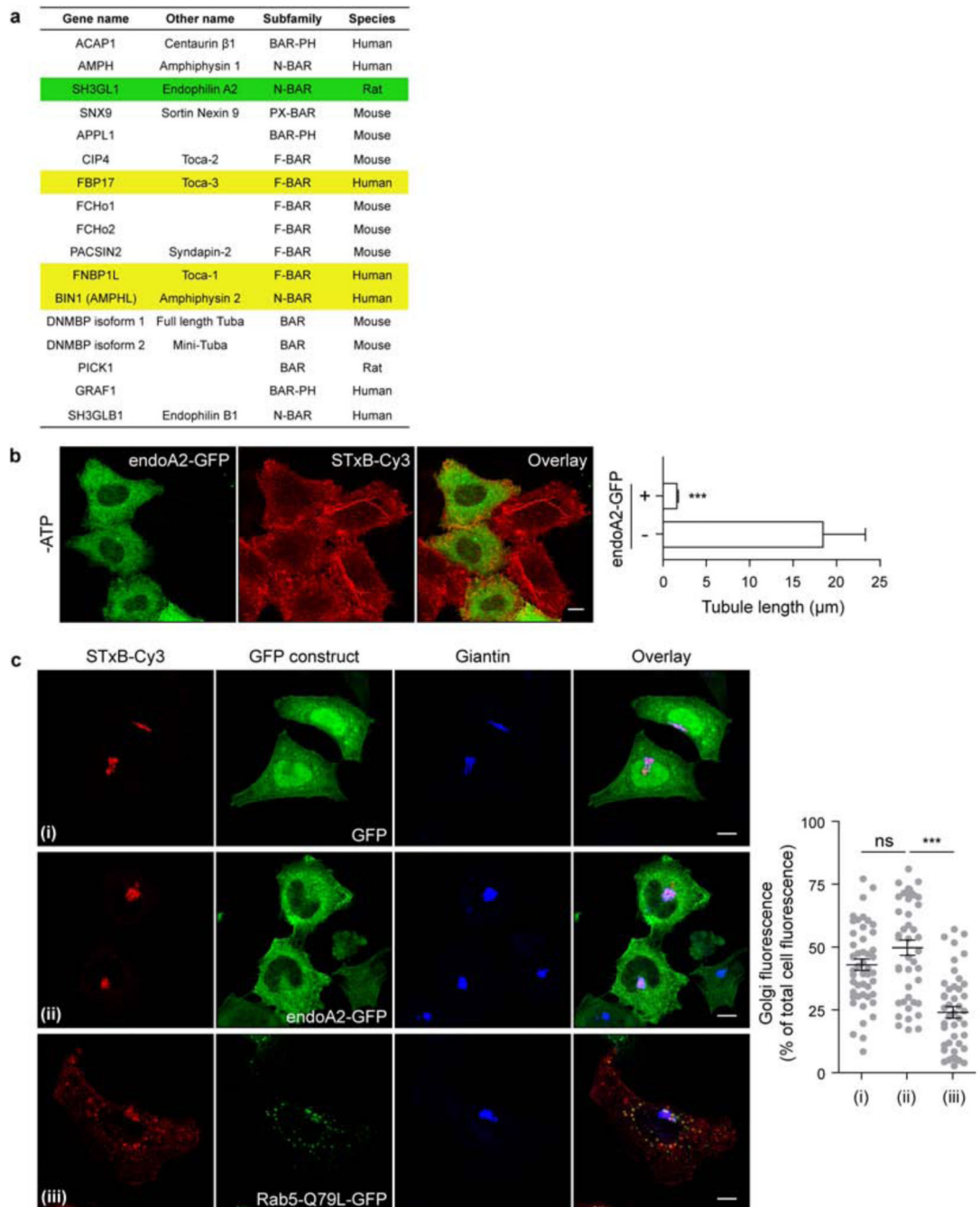
Extended Data Figure 1. Screening of BAR domain protein library
a, Listing of BAR domain proteins that were tested in our localization screen. Briefly, 24 hours after transfection of HeLa cells with fluorescent protein-tagged constructs, cells were ATP-depleted for 20 min, incubated for 20 min with 1 μM STxB-Cy3 or STxB-A488, fixed at 37°C, mounted, and viewed by confocal microscopy. The initial phenotype that was scored was BAR domain protein localization on STxB-induced plasma membrane

invaginations. TOCA1, TOCA3, and amphiphysin-2 (yellow underlay) colocalized with STxB on tubular structures (not shown). See below for endoA2 (green underlay). **b**, At variance with the expected phenotype, expression of GFP-tagged endoA2 (green) led to the disappearance of long STxB-induced plasma membrane invaginations (red). Tubule length was quantified in non transfected control cells (n=50), and endoA2-GFP expressing cells (n=59). Quantifications show means ± SEM of 2 independent experiments. *** $p<0.001$, two-tailed Mann-Whitney U test. **c**, STxB-Cy3 (50 nM, red) was incubated for 45 min at 37°C with cells expressing GFP (i), endoA2-GFP (ii), or Rab5-Q79L-GFP (iii). Expression of endoA2-GFP did not affect STxB trafficking to the Golgi/TGN membranes. n=48 for GFP expressing cells, n=43 for endoA2-GFP expressing cells, and n=46 for Rab5-Q79L–GFP expressing cells (2 independent experiments). Quantifications show means ± SEM. *** $p<0.001$, ns = non significant, Bonferroni's multiple comparison test. Scale bars: b,c=10 μm.

Extended Data Figure 2. Intracellular localization analysis of endoA2 and STxB

a–c, STxB is internalized in endoA2-GFP positive vesicles and induces the recruitment of endoA2-GFP to the plasma membrane. HeLaM cells stably expressing endoA2-GFP-FKBP (**a,c**), or HeLa cells transiently expressing endoA2-GFP (**b**) were incubated continuously at 37°C respectively with 0.2 μM STxB-Cy5 or 0.5 μM STxB-Cy3. Observation by live cell imaging using a spinning disk microscope (**a,c**) or TIRFM (**b**). **a**, STxB endocytosis. Image series of 170 sec (for the complete sequence, see Supplementary information, Video V1). Arrows show the formation in the cell periphery of STxB-Cy5 and endoA2-GFP positive

vesicles that move into cells. **b**, Kymographs of HeLa cells transiently expressing endoA2-GFP in the absence (−) or presence (+) of STxB-Cy3. Quantification from TIRFM recordings of endoA2-GFP spot lifetime (−STxB, n=1768 events; +STxB, n=144 events; 3 independent experiments; *** p<0.001, two-tailed Mann-Whitney U test). **c**, Plasma membrane recruitment of endoA2. STxB-Cy5 was added 15 sec after the beginning of image acquisition. Two time points are shown (for the complete sequence, see Supplementary information, Video V2): before STxB addition (− STxB, 0 sec) and after STxB addition (+ STxB, + 80 sec). A striking recruitment of endoA2-GFP to the plasma membrane was observed (white arrowheads). Fluorescence intensities along plasma membrane segments of endoA2-GFP and STxB-Cy5 were followed over time (means ± SEM, n=6 cells, 3 independent experiments). Note that both rose in a similar manner. **d–i**, EndoA2 and Shiga toxin poorly colocalize with markers of clathrin-mediated endocytosis. All images show live cell TIRF microscopy recordings. **d**, HeLa cells were transfected with plasmids expressing endoA2-GFP and μ2-mCherry. The overlap between both markers was very small. **e**, The genome-edited cell line SK-MEL-2 expressing LCa-mRFP was transfected transiently with endoA2-GFP plasmid. Again, both markers showed very little overlap. **f**, HeLa cells were transfected with plasmids expressing endoA2-GFP and DNM2-mRFP. A substantial overlap was observed between both markers. For **d–f**, quantifications are reported in Fig. 1d. **g–i**, HeLa cells transiently expressing mRFP-LCa (**g**) or μ2 -mCherry (**h**), and the genome-edited cell line SK-MEL-2 expressing LCa-mRFP (**i**) were continuously incubated with 0.5 μM STxB-A488 for 5 min at 37°C. Note the weak overlap between STxB and the other markers. **j**, Quantification of colocalization for **g–i**. Means ± SEM of the following numbers of cells: mRFP-Lca, n=11; μ2-mCherry, n=6; LCa-mRFP, n=19. 2 independent experiments. *** p<0.001, Bonferroni's multiple comparison test. Scale bars: a,c-i=2 μm.
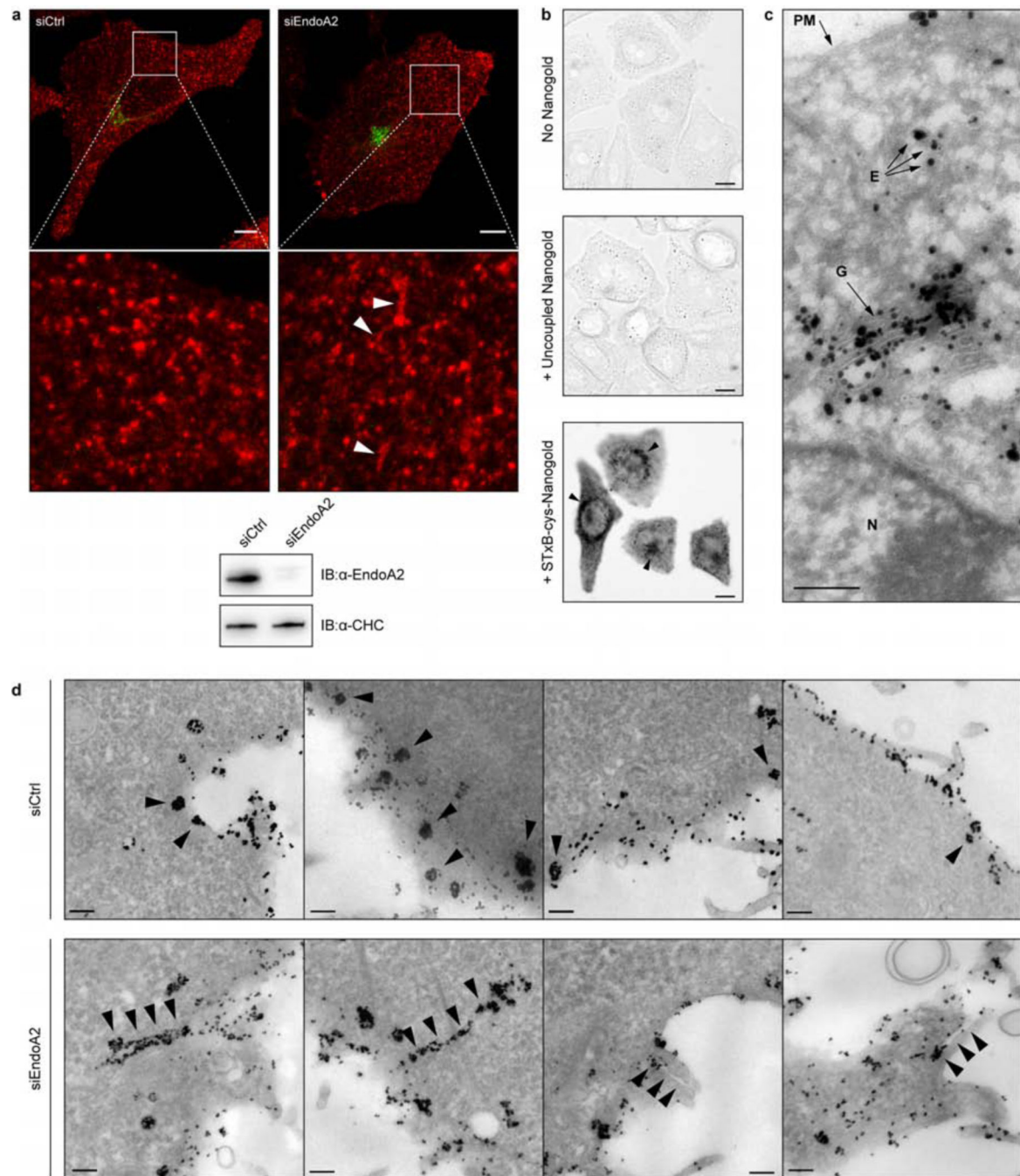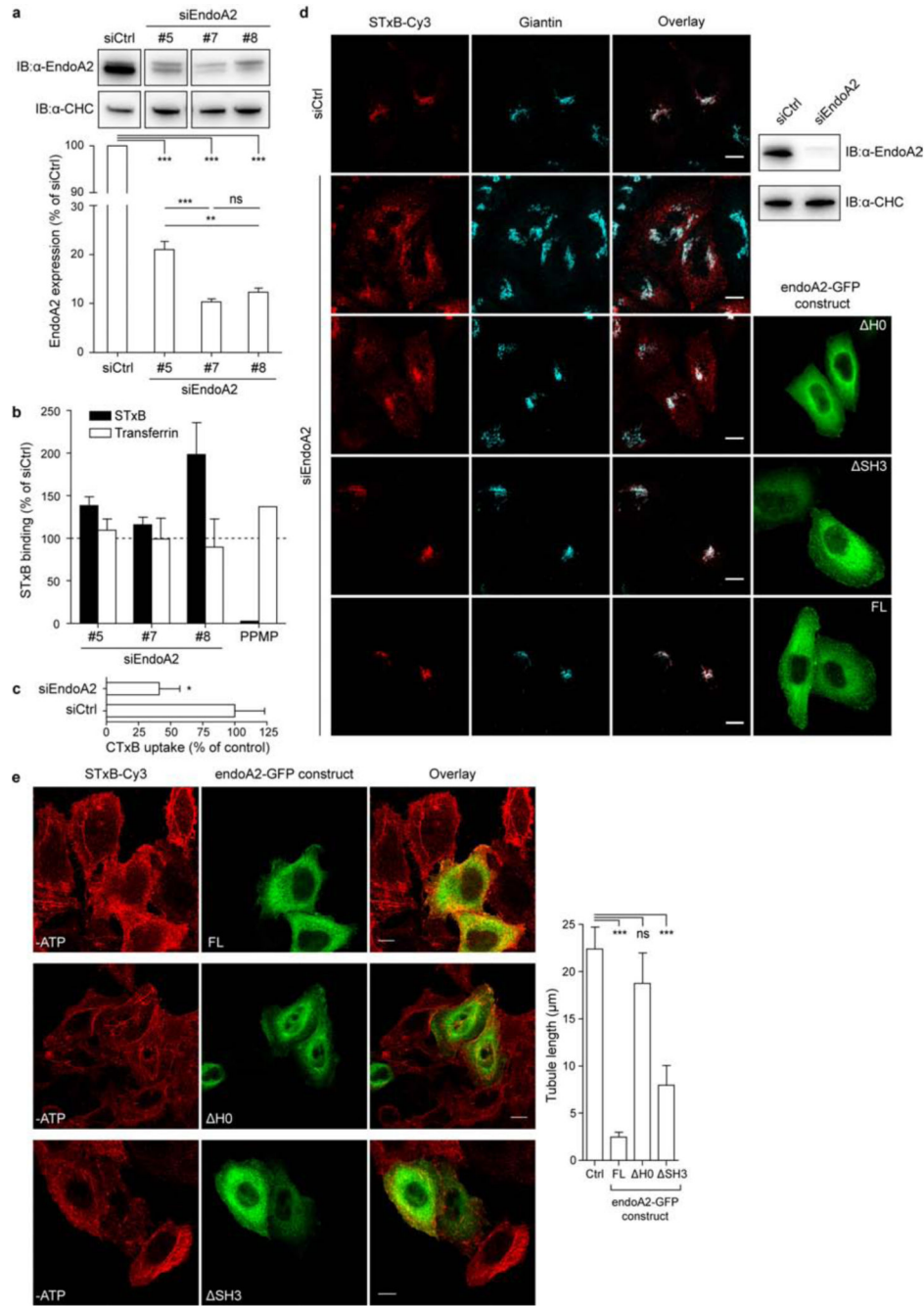
Extended Data Figure 3. Effect of endoA2 depletion on Shiga toxin endocytosis at early times of uptake

a, After binding on ice for 30 min, STxB-Cy3 (50 nM, red) was incubated for 5 min at 37°C with HeLa cells that had been transfected with negative control siRNAs (18 images), or siRNAs against endoA2 (23 images). After fixation, Golgi membranes were labeled with antibodies against giantin (green). Note the presence of short STxB-containing tubules (arrowheads) in the endoA2 depletion condition. The Western blot documents the efficiency of endoA2 depletion. Clathin heavy chain (CHC) was used as a loading control. **b–c**,

Characterization of STxB conjugates with monofunctionalized nanogold. **b**, HeLa cells were incubated for 45 min at 37°C in the indicated conditions, fixed, treated for silver enhancement, and viewed by transmission light microscopy. Note the strong perinuclear signal (arrowheads) that was visible only when cells were incubated with STxB-nanogold (113 images). **c**, HeLa cells were incubated for 45 min at 37°C with STxB-nanogold, fixed, treated for silver enhancement, and viewed by electron microscopy after sectioning (32 images). Note the strong signal in the Golgi region (G), which validated the functionality of the conjugate. Some STxB-nanogold could still be seen at the plasma membrane (PM) and in endosomes (E). N, nucleus. **d**, HeLa cells were transfected with negative control siRNAs, or siRNAs against endoA2, incubated for 30 min on ice with nanogold-coupled STxB, shifted for 5 min to 37°C, and then fixed. Silver enhancement was used to enlarge nanogold particles. Note that STxB-containing invaginations (arrowheads) were much longer in endoA2-depleted cells than in negative control siRNA-transfected cells. Quantification in shown in Fig. 2b (see legend for cell numbers). Scale bars: a,b=10 μm, c=200 nm, d=100 nm.

Extended Data Figure 4. Effect of endoA2 depletion on STxB and CTxB uptake, and rescue with endoA2 mutants

a, Efficiency of endoA2 depletion with different siRNA sequences. HeLa cells were transfected with 3 different siRNA sequences against human endoA2 (#5, #7 and #8). The efficiency of endoA2 depletion was monitored by Western blotting with antibodies against endoA2. Negative control siRNA-transfected cells were used for comparison. The Western signal for clathrin heavy chain (CHC) served as loading control. Quantification shows means ± SEM (n=3 independent experiments). ** p<0.01, *** p<0.001, ns = non significant

(Bonferroni's multiple comparison test). Trafficking studies on these cells are reported in Fig. 2c. **b**, Effect of endoA2 depletion on STxB binding to cells. Hela cells were transfected with siRNAs as in **a**, detached, incubated for 30 min on ice with 1 μM STxB-A488 and 10 μg/ml Tf-A647, washed, and analyzed by FACS. Cells treated with the glycosylceramide synthase inhibitor PPMP were used as a control for signal specificity. Means ± SEM of 3 independent experiments are shown (except for PPMP which was done twice). The increased STxB binding with siRNA #8 is not explained at this stage. These cell surface binding data serve as controls for the sulfation experiment of Fig. 2c. **c**, EndoA2 functions in CTxB uptake. CTxB (5 nM) uptake assay (*n*=3 independent experiments) after 10 min at 37°C in conditions of endoA2 depletion (* p<0.05, two-tailed t-test). As opposed to STxB, CTxB could be removed from the plasma membrane by acid washes, and endocytosis could therefore be measured directly using a plate reader assay (see Extended Methods in Supplementary information). **d**, STxB trafficking rescue experiment under endoA2 depletion conditions. HeLa cells were transfected with negative control siRNAs, or siRNAs against endoA2. After 48 hours, endoA2-depleted cells were transfected for 24 hours with siRNA-resistant expression vectors coding for: endoA2 ΔH0-GFP (ΔH0), endoA2 ΔSH3-GFP (ΔSH3), or full-length wild-type endoA2-GFP (FL). STxB-Cy3 (50 nM, red) was incubated with these cells for 45 min at 37°C (for quantification and statistical data, see Fig. 2d). The H0 helix deletion mutant did not rescue STxB transport to perinuclear Golgi/TGN membranes, as opposed to wild-type endoA2 and endoA2 ΔSH3. The Western blot documents the efficiency of endoA2 depletion in siRNA-transfected cells. Clathin heavy chain (CHC) was used as a loading control. **e**, Effect of endoA2 mutants on STxB-induced membrane invaginations. Non transfected HeLa cells (Ctrl) or cells expressing GFP-tagged full-length wild-type endoA2 (FL), H0 helix deletion mutant (ΔH0), or SH3 domain deletion mutant (ΔSH3) were ATP-depleted and incubated for 10 min at 37°C with 0.5 μM STxB-Cy3. Tubule length was quantified (Ctrl, *n=277* in 102 cells; FL, *n*=90 in 15 cells; ΔH0, *n*=183 in 48 cells; ΔSH3, *n=164* in 36 cells). 2 independent experiments. Quantifications show means ± SEM. *** p<0.001, ns = non significant, Bonferroni's multiple comparison test. Scale bars: d,e=10 μm.
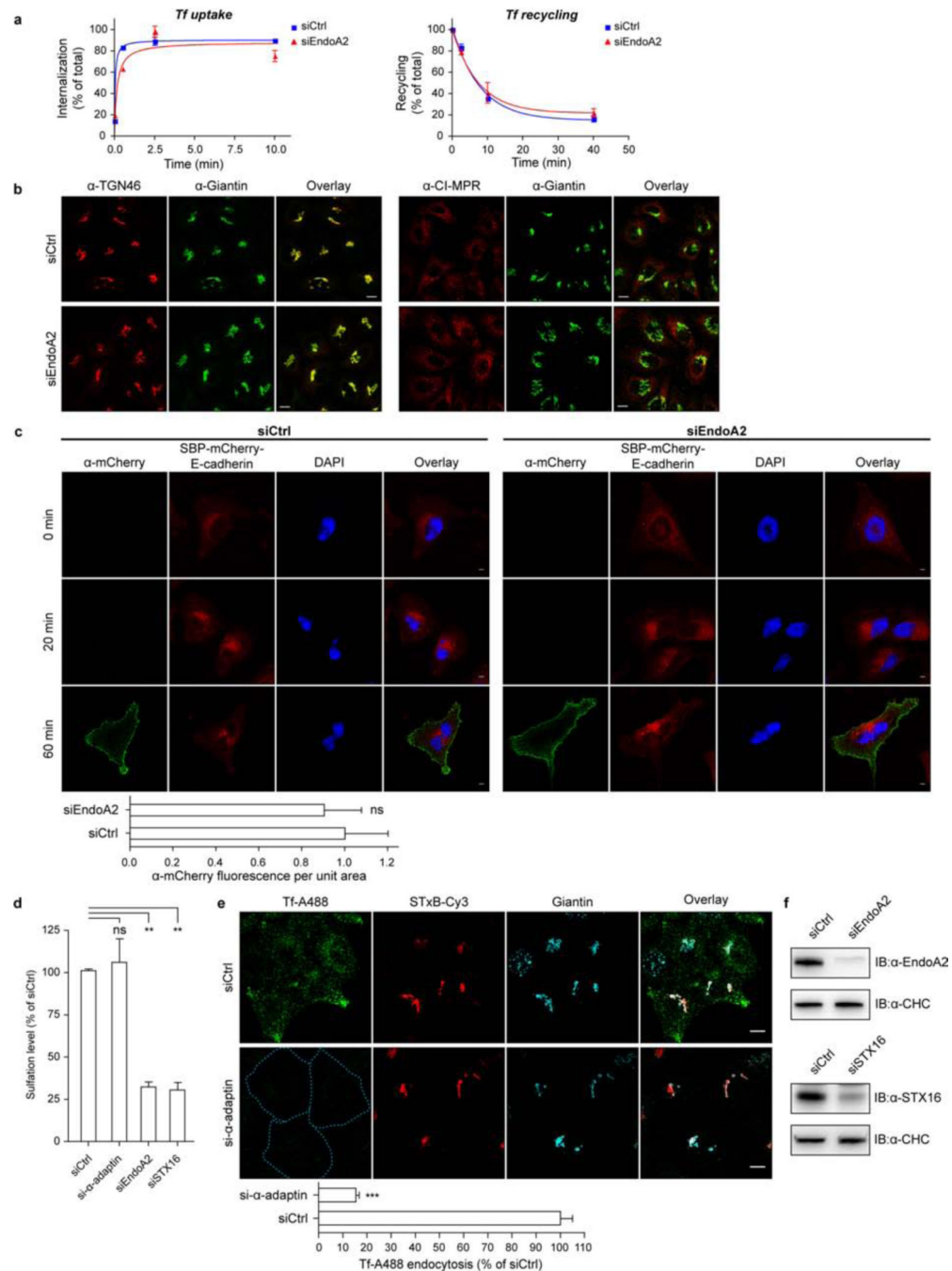
Extended Data Figure 5. Intracellular trafficking analysis

a–c, EndoA2 depletion does not affect general trafficking processes. All experiments were performed on negative control siRNA transfected cells, and on cells that were depleted for endoA2. **a**, Transferrin uptake (left, *n*=3) and recycling (right, *n*=4). EndoA2 depletion did not affect any of these processes. Quantifications show means ± SEM of the indicated numbers of independent experiments. **b**, Steady-state localization of TGN46 and CI-MPR (red), as analyzed by immunofluorescence. Golgi membranes were labeled with antibodies against giantin (green). EndoA2 depletion did not affect the steady-state localization of these

markers (TGN46 in siCtrl or siEndoA2 cells: 12 images; CI-MPR in siCtrl or siEndoA2 cells: 10 images; 2 independent experiments). **c**, Anterograde trafficking of E-cadherin. After release from endoplasmic reticulum, SBP-mCherry-E-cadherin protein was detected at the cell surface with anti-mCherry antibodies (0, 20 and 60 min time points). After 60 min, the relative means ($\pm$ SEM) of anti-mCherry fluorescence per unit area were quantified for control (6 images, 87 cells) and endoA2-depleted cells (6 images, 81 cells). 3 independent experiments. No significant difference was observed using a two-tailed t-test ($p>0.05$). **d–f**, Depletion of α-adaptin does not affect Shiga toxin trafficking. All experiments were performed on negative control siRNA transfected cells, and on cells that were depleted for the indicated proteins. Quantifications show means $\pm$ SEM. **d**, Sulfation analysis of retrograde STxB transport (3 independent experiments). HeLa cells in the indicated conditions were incubated for 20 min at 37°C with STxB-Sulf$_2$ in the presence of radioactive sulfate, and sulfated STxB-Sulf$_2$ was measured by autoradiography. Note that α-adaptin depletion did not affect sulfation of STxB-Sulf$_2$, while depletion of endoA2 or syntaxin-16 (STX16) had a strong effect. ** $p<0.01$, ns = non significant (Bonferroni's multiple comparison test). **e**, Immunofluorescence analysis. HeLa cells in the indicated conditions were incubated for 45 min at 37°C with 0.05 μM STxB-Cy3 (red). During the last 10 min, 10 μg/ml Tf-A488 (green) were added in the growth medium. Cells were placed on ice, and cell surface exposed Tf was removed by acid washes. After fixation, cells were labeled for giantin (blue). Note that α-adaptin depletion strongly inhibited Tf uptake, but not retrograde transport of STxB to TGN/Golgi membranes. Tf uptake was quantified for control (5 images, 102 cells) and α-adaptin-depleted cells (5 images, 108 cells). 2 independent experiments. *** $p<0.001$ (two-tailed t-test). **f**, siRNA-mediated depletion of endoA2 and of syntaxin-16 was analyzed by Western blotting. Clathrin heavy chain (CHC) was used as loading control. Scale bars: b,c,e=10 μm.
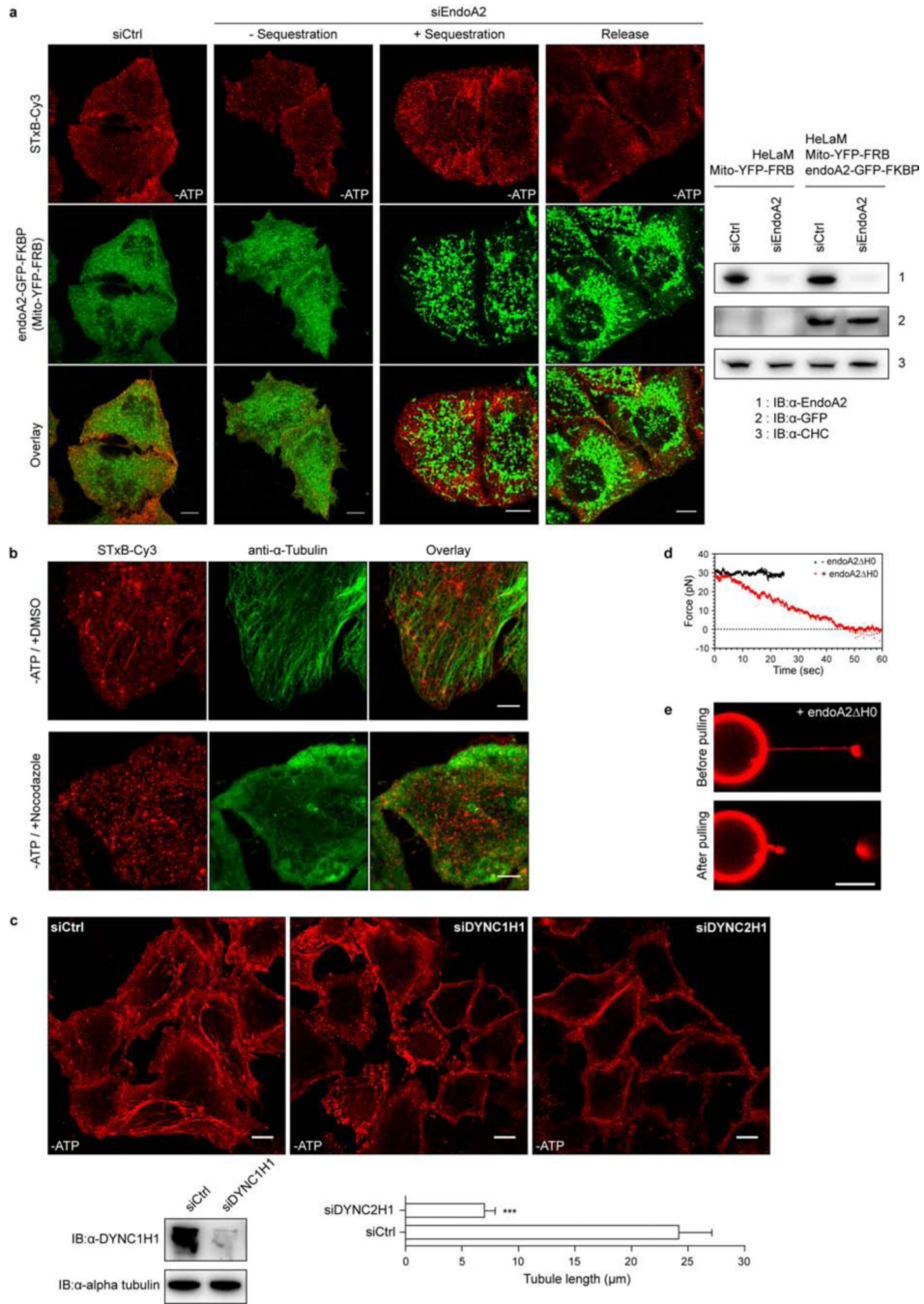
Extended Data Figure 6. Cell and model membrane experiments

a, Knocksideways. HeLaM cells stably expressing Mito-YFP-FRB and rat endoA2-GFP-FKBP (green) were transfected with negative control siRNAs (siCtrl), or siRNAs against human endoA2 (siEndoA2) that did not cross with the rat sequence. STxB-Cy3 (0.5 μM, red) was incubated for 15 min at 37°C with ATP-depleted cells. The cells were then fixed at 37°C, and viewed by confocal microscopy. Quantification of tubule formation and cell numbers are shown in Fig. 3a. Note that STxB-induced tubule length reversibly increased after endoA2-GFP-FKBP sequestration. The depletion of endogenous human endoA2, and

the expression of GFP-FKBP-tagged rat endoA2 were assessed by Western blotting with anti-endoA2 and anti-GFP antibodies, respectively. Western blotting against clathrin heavy chain (CHC) was used as loading control. **b–c**, Interfering with microtubules or dynein motors strongly affects STxB-induced tubule length. **b**, HeLa cells were incubated for 1 hour at 37°C with DMSO (+ DMSO) or 10 μM nocodazole (+ nocodazole), ATP-depleted for 20 min, and then incubated for 10 min at 37°C with 0.5 μM STxB-Cy3 (red) in the same conditions. Labeling with an antibody against a-tubulin (green) was used to visualize the efficiency of nocodazole treatment. Long tubular structures containing STxB could not be detected after incubation with nocodazole (−ATP/+DMSO: 18 images; -ATP/+Nocodazole: 16 images; 3 independent experiments). **c**, Heavy chains of cytoplasmic dyneins (DYNC1H1 and DYNC2H1) were depleted from HeLa cells with siRNAs. Cells were ATP-depleted and then incubated for 10 min at 37°C with 0.5 μM STxB-Cy3 (red). The presence of long STxB-induced tubules was strongly decreased under these conditions. Tubule length was quantified for negative control siRNA treated cells (siCtrl, *n*=188) and for DYNC2H1 depleted cells (siDYNC2H1, *n=165). 2* independent experiments. Quantifications show means ± SEM. *** p<0.001, two-tailed Mann-Whitney U test. The Western blot documents the efficiency of DYNC1H1 depletion. **a**-tubulin was used as a loading control. **d–e**, Model membranes experiments. **d**, Measurement of tube pulling force over time in the absence (−endoA2 H0) or presence of endoA2 H0 mutant (+ endoA2 H0, 7 μM in injection pipette). **e**, Scission experiments with tethers that were coated with endoA2 H0. Scale bars: a,c=10 μm, b,e=5 μm.
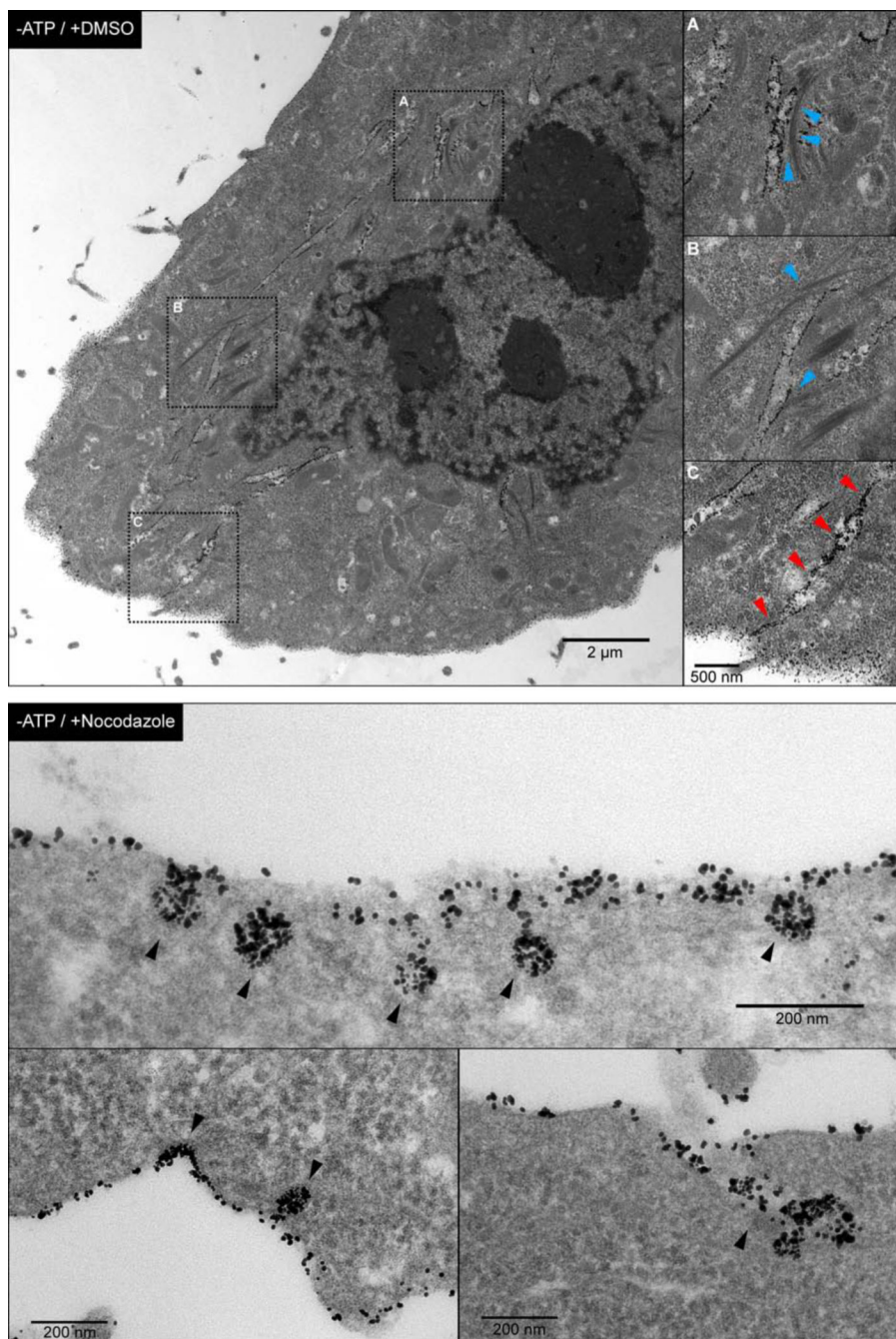
Extended Data Figure 7. Electron microscopy of STxB-nanogold on ATP-depleted cells following treatment with nocodazole

HeLa cells were treated for 1 hour at 37°C with DMSO (top panel) or 10 μM nocodazole (bottom panel). During the last 20 min, ATP was depleted. Cells were then incubated for 10 min with STxB-nanogold in the continued presence of inhibitors, fixed, and prepared for electron microscopy. In the DMSO condition (top panel), long tubular structures connected to cells surface were observed (magnified views in right insets, red arrowheads in C), as expected from light microscopy experiments. These structures were in close proximity with microtubules, as indicated with blue arrowheads in magnifications A and B. In the

nocodazole condition (lower panel), STxB-induced plasma membrane invaginations were still present (arrowheads), but much shorter (mean length of 118.2 ± 7.0 nm, n=109 invaginations; 0.90 ± 0.12 invaginations/μm of plasma membrane, n=28 images; 3 independent experiments) than in the absence of the compound. Scale bar sizes are indicated on each micrograph.
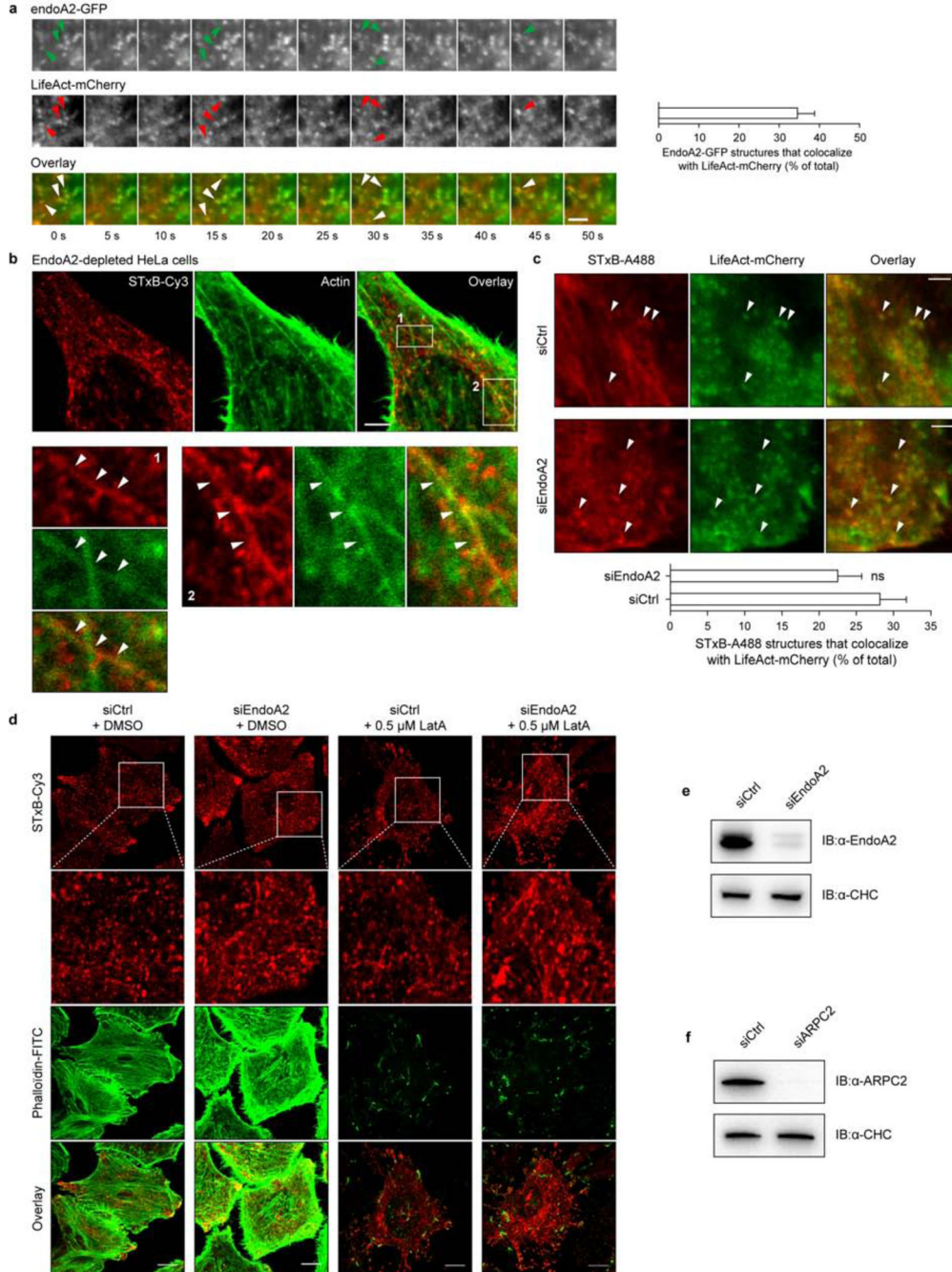
Extended Data Figure 8. Actin and endoA2

a–c, EndoA2 codistribution with actin. **a**, HeLa cells transiently co-expressing endoA2-GFP and mCherry-LifeAct were observed by time-resolved TIRF microscopy. The panel shows acquisitions at the plasma membrane that were taken at 5 sec intervals. Arrowheads point out examples of structures on which endoA2 and actin colocalize in a dynamic manner. Quantification of colocalization of endoA2-positive structures with LifeAct is presented as mean ± SEM (n=7 cells, 2 independent experiments). **b**, EndoA2-depleted HeLa cells were incubated continuously for 5 min at 37°C with 0.5 μM STxB-Cy3. After fixation, actin filaments were stained with Phalloidin-FITC. Arrowheads indicate STxB-induced tubules that are decorated by actin. **c**, HeLa cells transfected with negative control or endoA2 siRNAs (siCtrl or siEndoA2, respectively) and transiently expressing mCherry-LifeAct were observed by TIRF microscopy after addition of 0.5 μM STxB-Cy3 at 37°C. Arrowheads point out examples of structures on which STxB and actin colocalize. Quantification of colocalization of STxB-positive structures with LifeAct is presented as means ± SEM (n=6 cells, 2 independent experiments). ns = non significant (two-tailed t-test). **d–e**, Analysis of STxB-induced plasma membrane invaginations in function of endoA2 depletion and/or actin perturbation. **d**, HeLa cells were transfected with negative control siRNAs or with siRNAs against endoA2, and treated or not with 0.5 μM latrunculin-A. The cells were then incubated continuously for 5 min at 37°C in the presence of 0.5 μM STxB-Cy3 (red), fixed, and labeled with phalloïdin (green). The quantification of STxB tubule length is shown in Fig. 4a. Note that tubule length increased with combined treatments (siCtrl+DMSO: 22 images; siEndoA2+DMSO: 11 images; siCtrl+LatA: 14 images; siEndoA2+LatA: 14 images). **e**, Depletion of endoA2 was analyzed by Western blotting. Clathrin heavy chain (CHC) was used as loading control. **f**, Efficiency of ARPC2 depletion. HeLa cells were transfected for 72 hours with a smartpool of 4 siRNA sequences against ARPC2. The efficiency of ARPC2 depletion was monitored by Western blotting with antibodies against ARPC2. The Western signal for clathrin heavy chain (CHC) served as loading control. Corresponds to experiments in Fig. 4a. Scale bars: a,c=2 μm, b=5 μm, d=10 μm.
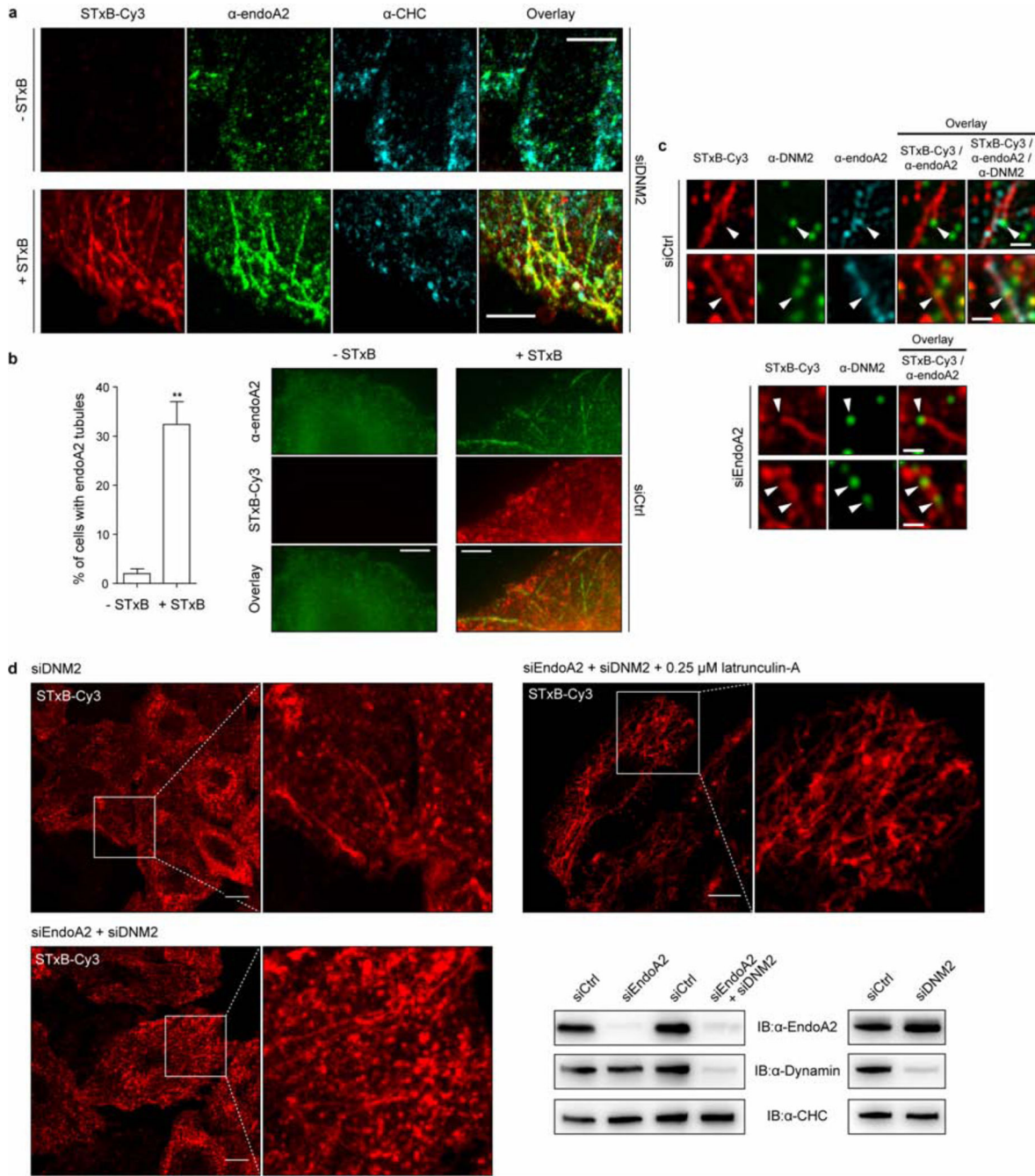
Extended Figure 9. Combined effects of interference with endoA2, dynamin and actin on STxB-induced membrane invaginations

a–c, Endogenous endoA2 and dynamin are found on STxB-induced plasma membrane invaginations. **a**, Dynamin-2 was depleted from cells (siDNM2), which were then incubated continuously for 5 min at 37°C in the presence or absence of 0.5 μM STxB-Cy3 (red), fixed, labeled for the indicated markers, and analyzed by confocal microscopy. Note that endoA2-containing tubules (green) were seen only in the presence of STxB. No overlap was observed with clathrin (blue). –STxB: representative of 15 images; +STxB: representative of

35 images; 2 independent experiments. **b**, Experiment as in (**a**) on wild-type cells that were analyzed by wide field microscopy. As above, endoA2 (green) was found on tubular structures only in the presence of STxB (red). The quantification shows means ± SEM of 3 independent experiments on 234 cells without STxB (– STxB) and 921 cells with STxB (+ STxB). ** p<0.01, two-tailed t-test. **c**, Negative control siRNA transfected HeLa cells and endoA2-depleted cells were incubated for 5 min at 37°C in the presence of 0.5 μM STxB-Cy3 (red). Endogenous endoA2 (blue) and dynamin (green, arrowheads) were labeled with specific antibodies, detected by immunofluorescence, and viewed by structured illumination microscopy. Note that dynamin localized in spots on STxB-induced invaginations, while endoA2 distributed in a continuous manner. **d**, Analysis of STxB-induced plasma membrane invaginations in function of endoA2 and dynamin-2 depletion, and actin perturbation. HeLa cells were depleted for dynamin-2 alone, dynamin-2 in combination with endoA2, or both depletions in combination with 0.25 μM latrunculin-A treatment, as indicated. These cells were then incubated continuously for 5 min at 37°C with 0.5 μM STxB-Cy3 (red), fixed at 37°C, and viewed by confocal microscopy. Note that the tubulation phenotype increased with each additional interference modality (siDNM2: 21 images; siEndoA2+siDNM2: 15 images; siEndoA2+siDNM2+LatA: 16 images; 2 independent experiments). The quantification of tubule length in the different experimental conditions of this figure is shown in Fig. 4a. The depletion of dynamin-2 and endoA2 was validated by immunoblotting. Clathrin heavy chain (CHC) was used as loading control. Scale bars: a,b=5 μm, c=0.5 μm, d=10 μm.
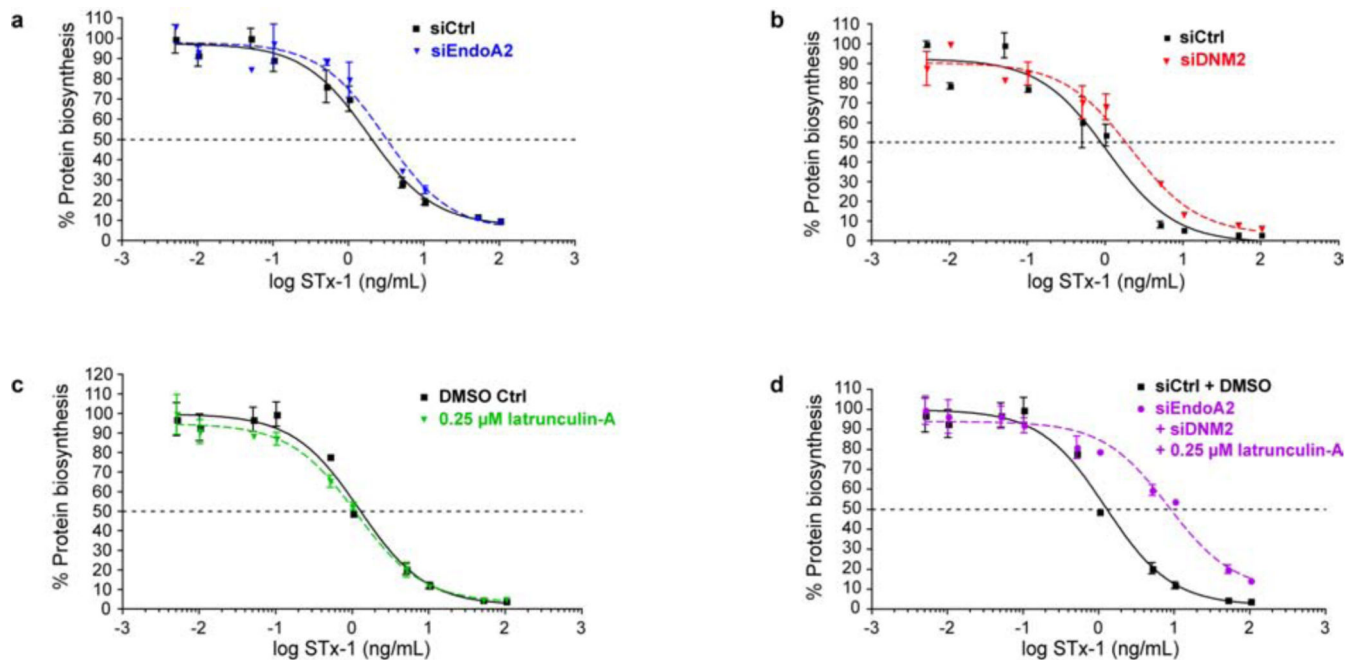
Extended Data Figure 10. Intoxication curves

a–d, HeLa cells were depleted for endoA2 (**a**), dynamin-2 (**b**), incubated with 0.25 μM latrunculin-A (**c**), or submitted concomitantly to all three perturbations (**d**). These cells were then further incubated for 1 hour in the presence of increasing concentrations of STx-1, at

the end of which protein biosynthesis was measured. Note that only the triple treatment condition had a strong effect on cell intoxication. The protection factors determined on 4–13 independent experiments are shown in Fig. 4c. Error bars show the SEM.

Acknowledgements

References

1. Campelo F, Malhotra V. Membrane Fission: The Biogenesis of Transport Carriers. Ann. Rev. Biochem. 2012; 81(1):407–427. [PubMed: 22463692]

2. Shnyrova AV, et al. Geometric catalysis of membrane fission driven by flexible dynamin rings. Science. 2013; 339(6126):1433–1436. [PubMed: 23520112]

3. Morlot S, et al. Membrane shape at the edge of the dynamin helix sets location and duration of the fission reaction. Cell. 2012; 151(3):619–629. [PubMed: 23101629]

4. Faelber K, et al. Crystal structure of nucleotide-free dynamin. Nature. 2011; 477(7366):556–560. [PubMed: 21927000]

5. Sundborger A, et al. An endophilin-dynamin complex promotes budding of clathrin-coated vesicles during synaptic vesicle recycling. J. Cell Sci. 2011; 124(Pt 1):133–143. [PubMed: 21172823]

6. Neumann S, Schmid SL. Dual role of BAR domain-containing proteins in regulating vesicle release catalyzed by the GTPase, dynamin-2. J. Biol. Chem. 2013; 288(35):25119–25128. [PubMed: 23861397]

7. Howes MT, Mayor S, Parton RG. Molecules, mechanisms, and cellular roles of clathrin-independent endocytosis. Curr. Opin. Cell Biol. 2010; 22(4):519–527. [PubMed: 20439156]

8. Römer W, et al. Shiga toxin induces tubular membrane invaginations for its uptake into cells. Nature. 2007; 450:670–675. [PubMed: 18046403]

9. Mim C, Unger VM. Membrane curvature and its generation by BAR proteins. Trends Biochem. Sci. 2012; 37(12):526–533. [PubMed: 23058040]

10. Römer W, et al. Actin dynamics drive membrane reorganization and scission in clathrin-independent endocytosis. Cell. 2010; 140(4):540–553. [PubMed: 20178746]

11. Ewers H, et al. GM1 structure determines SV40-induced membrane invagination and infection. Nat. Cell Biol. 2010; 12:11–18. [PubMed: 20023649]

12. Milosevic I, et al. Recruitment of endophilin to clathrin-coated pit necks is required for efficient vesicle uncoating after fission. Neuron. 2011; 72(4):587–601. [PubMed: 22099461]

13. Llobet A, et al. Endophilin drives the fast mode of vesicle retrieval in a ribbon synapse. J. Neurosci. 2011; 31(23):8512–8519. [PubMed: 21653855]

14. Kononenko NL, et al. Clathrin/AP-2 mediate synaptic vesicle reformation from endosome-like vacuoles but are not essential for membrane retrieval at central synapses. Neuron. 2014; 82(5): 981–988. [PubMed: 24908483]

15. Amessou M, et al. Syntaxin 16 and syntaxin 5 control retrograde transport of several exogenous and endogenous cargo proteins. J. Cell. Sci. 2007; 120:1457–1468. [PubMed: 17389686]

16. Draper RK, Goda Y, Brodsky FM, Pfeffer SR. Antibodies to clathrin inhibit endocytosis but not recycling to the trans Golgi network in vitro. Science. 1990; 248(4962):1539–1541. [PubMed: 2163108]

17. Nesterov A, Carter RE, Sorkina T, Gill GN, Sorkin A. Inhibition of the receptor-binding function of clathrin adaptor protein AP-2 by dominant-negative mutant mu2 subunit and its effects on endocytosis. Embo J. 1999; 18(9):2489–2499. [PubMed: 10228163]

18. Robinson MS, Sahlender DA, Foster SD. Rapid inactivation of proteins by rapamycin-induced rerouting to mitochondria. Dev. Cell. 2010; 18(2):324–331. [PubMed: 20159602]

19. Campillo C, et al. Unexpected membrane dynamics unveiled by membrane nanotube extrusion. Biophys. J. 2013; 104(6):1248–1256. [PubMed: 23528084]

20. Cuvelier D, Derenyi I, Bassereau P, Nassoy P. Coalescence of membrane tethers: experiments, theory, and applications. Biophys. J. 2005; 88(4):2714–2726. [PubMed: 15695629]

21. Evans E, Yeung A. Hidden dynamics in rapid changes of bilayer shape. Chem. Phys. Lipids. 1994; 73:39–56.

22. Toba S, Watanabe TM, Yamaguchi-Okimoto L, Toyoshima YY, Higuchi H. Overlapping hand-over-hand mechanism of single molecular motility of cytoplasmic dynein. Proc. Natl. Acad. Sci. USA. 2006; 103(15):5741–5745. [PubMed: 16585530]

23. Hehnly H, Sheff D, Stamnes M. Shiga toxin facilitates its retrograde transport by modifying microtubule dynamics. Mol. Biol. Cell. 2006; 17(10):4379–4389. [PubMed: 16885418]

24. Meinecke M, et al. Cooperative recruitment of dynamin and BIN/amphiphysin/Rvs (BAR) domain-containing proteins leads to GTP-dependent membrane scission. J. Biol. Chem. 2013; 288(9):6651–6661. [PubMed: 23297414]

25. Johannes L, Römer W. Shiga toxins - from cell biology to biomedical applications. Nat. Rev. Microbiol. 2010; 8:105–116. [PubMed: 20023663]

26. Itoh T, et al. Dynamin and the actin cytoskeleton cooperatively regulate plasma membrane invagination by BAR and F-BAR proteins. Dev. Cell. 2005; 9(6):791–804. [PubMed: 16326391]

27. Roux A, Uyhazi K, Frost A, De Camilli P. GTP-dependent twisting of dynamin implicates constriction and tension in membrane fission. Nature. 2006; 441:528–531. [PubMed: 16648839]

28. Zha X, et al. Sphingomyelinase treatment induces ATP-independent endocytosis. J. Cell Biol. 1998; 140(1):39–47. [PubMed: 9425152]

29. Lizarraga F, et al. Diaphanous-related formins are required for invadopodia formation and invasion of breast tumor cells. Cancer Res. 2009; 69(7):2792–2800. [PubMed: 19276357]

30. Riedl J, et al. Lifeact: a versatile marker to visualize F-actin. Nat. Methods. 2008; 5(7):605–607. [PubMed: 18536722]

31. Jordan M, Schallhorn A, Wurm FM. Transfecting mammalian cells: optimization of critical parameters affecting calcium-phosphate precipitate formation. Nucleic Acids Res. 1996; 24(4):596–601. [PubMed: 8604299]

32. Montagnac G, et al. Decoupling of activation and effector binding underlies ARF6 priming of fast endocytic recycling. Curr. Biol. 2011; 21(7):574–579. [PubMed: 21439824]

33. Mallard, F.; Johannes, L. Shiga toxin B-subunit as a tool to study retrograde transport. Chapter 17. In: Philpott, D.; Ebel, F., editors. Methods Mol. Med. Shiga Toxin Methods and Protocols. Vol. 73. 2003. p. 209-220.

34. Gortat A, San-Roman MJ, Vannier C, Schmidt AA. Single point mutation in Bin/Amphiphysin/Rvs (BAR) sequence of endophilin impairs dimerization, membrane shaping, and Src homology 3 domain-mediated partnership. J. Biol. Chem. 2012; 287(6):4232–4247. [PubMed: 22167186]

35. Amessou, M.; Popoff, V.; Yelamos, B.; Saint-Pol, A.; Johannes, L. Measuring retrograde transport to the trans-Golgi network. Chapter 15: Unit 15.10. In: Bonifacino, Juan S., et al., editors. Curr. Protoc. Cell. Biol. John Wiley & Sons, Inc.; 2006.

36. Singh RD, et al. Selective caveolin-1-dependent endocytosis of glycosphingolipids. Mol. Biol. Cell. 2003; 14(8):3254–3265. [PubMed: 12925761]

37. Wolf AA, et al. Ganglioside structure dictates signal transduction by cholera toxin and association with caveolae-like membrane domains in polarized epithelia. J. Cell Biol. 1998; 141(4):917–927. [PubMed: 9585411]

38. Stechmann B, et al. Inhibition of retrograde transport protects mice from lethal ricin challenges. Cell. 2010; 141:231–242. (* corresponding authors). [PubMed: 20403321]

39. Robinson MS, Hirst J. Rapid inactivation of proteins by knocksideways. Curr. Protoc. Cell Biol. 2013; 61:11–17. 15 20.

40. Boncompain G, Perez F. Synchronizing protein transport in the secretory pathway. Chapter 15, Unit 15 19. Curr. Protoc. Cell Biol. 2012

41. Pautot S, Frisken BJ, Weitz DA. Engineering asymmetric vesicles. Proc. Natl. Acad. Sci. USA. 2003; 100(19):10718–10721. [PubMed: 12963816]

42. Pontani LL, et al. Reconstitution of an actin cortex inside a liposome. Biophys. J. 2009; 96(1):192–198. [PubMed: 19134475]

43. Sorre B, et al. Nature of curvature coupling of amphiphysin with membranes depends on its bound density. Proc. Natl. Acad. Sci. USA. 2012; 109(1):173–178. [PubMed: 22184226]

44. Bolte S, Cordelieres FP. A guided tour into subcellular colocalization analysis in light microscopy. J. Microsc. 2006; 224(Pt 3):213–232. [PubMed: 17210054]
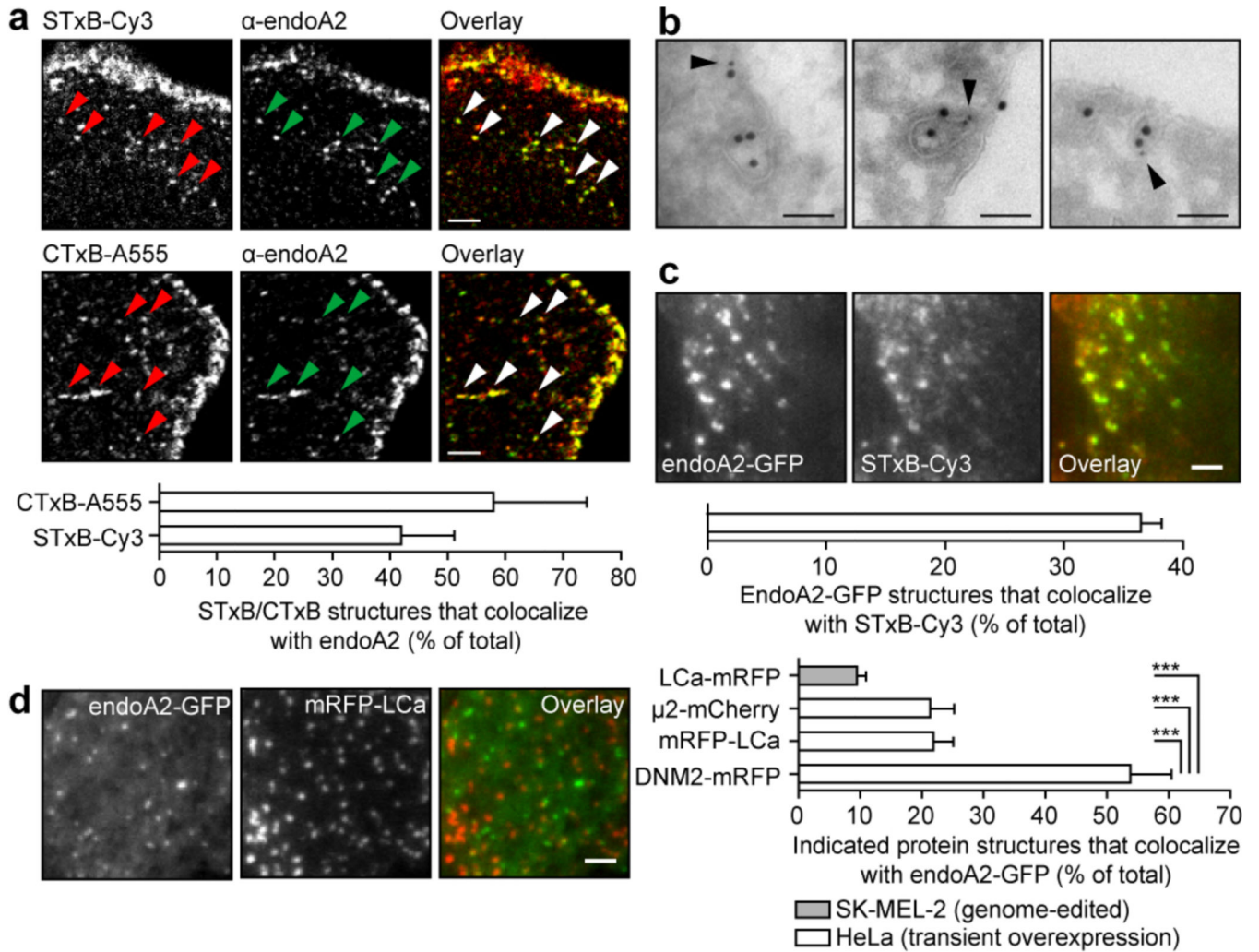
Figure 1. EndoA2 localization to endocytic pathways

Quantifications show means ± SEM. All conditions: incubation for 5 min at 37°C (except if stated otherwise). **a**, BSC-1 cells with 50 nM STxB-Cy3 (*n*=20 cells) or 5 nM CTxB-Alexa555 (*n*=50 cells) for 3 min at 37°C, and labeling for endoA2 (3 independent experiments). **b**, Cryoelectron microscopy on HeLa cells incubated with 0.5 μM STxB: STxB 15 nm, endoA2 (arrows) 10 nm (representative of 50 images). **c**, HeLa cells transiently expressing endoA2-GFP incubated with 0.5 μM STxB-Cy3 and analyzed by TIRFM (*n*=25 cells, 3 independent experiments). **d**, Colocalization analysis by TIRFM of endoA2 with the indicated markers (transient expression in HeLa cells: DNM2-mRFP, *n*=10; mRFP-LCa, *n*=8; μ2-mCherry, *n*=12; genome-edited SK-MEL-2: LCa-mRFP, *n*=8; 2 independent experiments; *** $p<0.001$, Bonferroni's multiple comparison test). Scale bars: a,c,d=2 μm, b=100 nm.
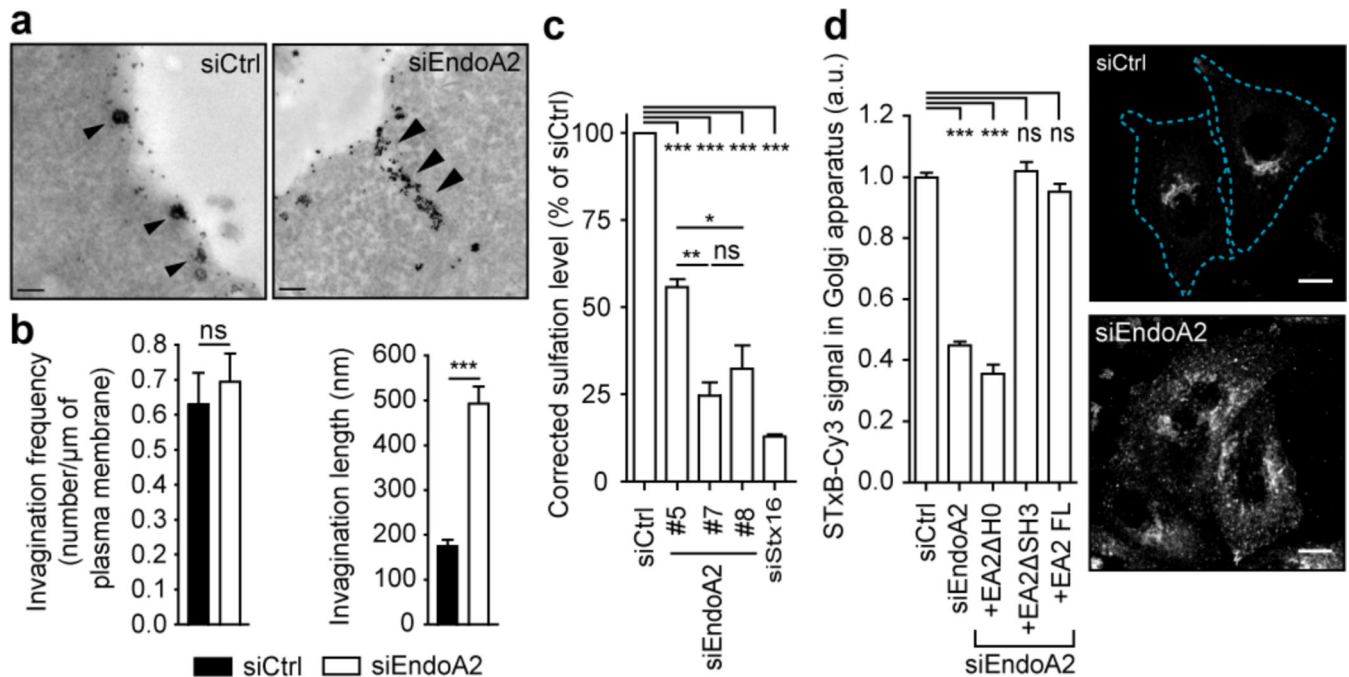
Figure 2. EndoA2 functions in Shiga toxin uptake

Quantifications show means ± SEM. **a**, 5 min incubation at 37°C of control (siCtrl) or endoA2-depleted (siEndoA2) HeLa cells with nanogold-coupled STxB (arrowheads indicate invaginations; representative images of numbers of cells as shown in **b**). **b**, Frequency (siCtrl, *n*=25 cells; siEndoA2, *n*=27 cells) and length (siCtrl, *n*=149 tubules; siEndoA2, *n*=138 tubules) of STxB-containing invaginations on experiments as in (**a**) (ns = non significant, *** $p<0.001$, two-tailed Mann-Whitney U test). **c**, Sulfation analysis (*n*=3 independent experiments) on HeLa cells (ns = non significant, * $p<0.05$, ** $p<0.01$, *** $p<0.001$, Bonferroni's multiple comparison test). **d**, Rescue experiment on endoA2-depleted HeLa cells. Incubation for 45 min at 37°C with 50 nM STxB-Cy3. One a.u. corresponds to 78.7 ± 1.2% of STxB in Golgi area. Numbers of cells: siCtrl, *n*=145; siEndoA2, *n*=190; siEndoA2+EA2 H0, *n*=46; siEndoA2+EA2 SH3, *n*=31; siEndoA2+EA2 FL, *n*=56; 2 independent experiments; ns = non significant, *** $p<0.001$, Bonferroni's multiple comparison test. Scale bars: a=100 nm, d=10 μm.
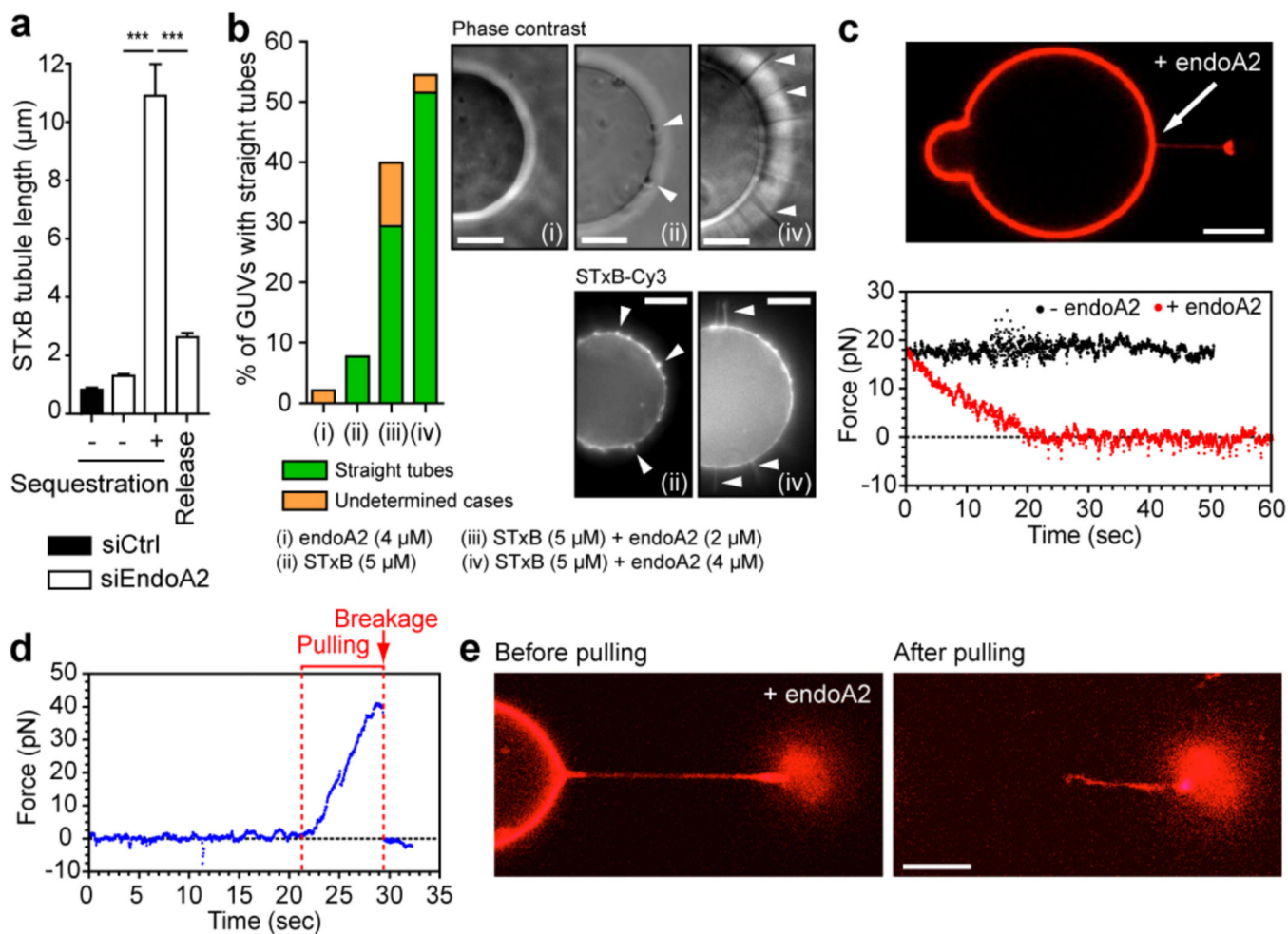
Figure 3. Model membrane experiments
a, Knocksideways on ATP-depleted HeLaM cells in control (siCtrl) or endoA2-depletion conditions (siEndoA2). Incubations for 15 min at 37°C with STxB (0.5 μM). Means ± SEM of the following numbers of tubules: siCtrl, *n*=65 (30 cells); –sequestration, *n*=101 (52 cells); +sequestration, *n*=313 (131 cells); release, *n*=626 (187 cells). 2 independent experiments. *** p<0.001, Dunn's multiple comparison test. **b**, Inverse emulsion technique in conditions i to iv, as indicated. Number of vesicles: i, *n*=46; ii, *n*=39; iii, *n*=17; iv, *n*=32; 3 independent experiments. Arrows point to tubular structures. **c–e** Nanotube tethers. **c**, Tube retraction force in presence (1 μM) or absence of endoA2. **d,e**, Measurement of retraction force over time upon stepwise elongation at 0.5 μm/s of an endoA2-scaffolded tube (**d**), and pulling force-driven scission (**e**). Scale bars: b=10 μm, c,e=5 μm.
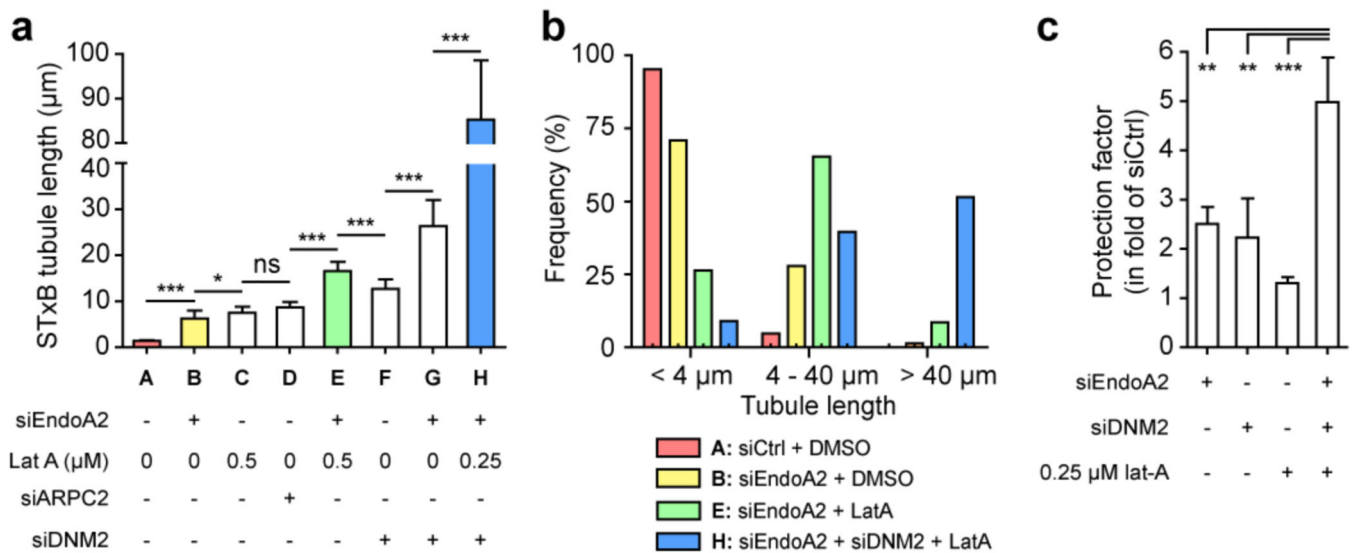
Figure 4. Additive effects of scission factors

Quantifications show means ± SEM. **a**, Incubation of HeLa cells for 5 min at 37°C with STxB-Cy3 (0.5 μM). Determination of tube length on fixed cells (number of tubules per condition: A, *n*=254; B, *n*=79; C, *n*=94; D, *n*=146; E, *n*=118; F, *n*=338; G, *n*=131; H, *n*=115; 2 independent experiments; ns = non significant, * p<0.05, *** p<0.001, Dunn's multiple comparison test). **b**, Frequency distribution of tubules according to length (conditions as in **a**). **c**, Intoxication analysis. Protection factors on 4 to 13 independent experiments per condition (*** p<0.001, Bonferroni's multiple comparison test).